

Microstructures and Creep Properties of Type 316LN Stainless Steel Weld Joints



A.R. PAVAN, T. SAKTHIVEL, B. ARIVAZHAGAN, M. VASUDEVAN,
and B.R. VAISHNAVI KRUPA

In the present investigation, creep deformation and rupture behavior of type 316LN stainless steel weld joints fabricated from hotwire tungsten inert gas (HW-TIG), activated-TIG (A-TIG), and hybrid laser metal inert gas (HLM) welding processes were studied. The creep testing was carried out at 923 K under various stress levels. The weld joints have undergone a higher rate of deformation and exhibited lower creep rupture life as compared to that of the base metal. The welding process significantly influenced the delta (δ)-ferrite content in the weld metal of stainless steel weld joints [A-TIG (1.7 ferrite number (FN)), HLM (1.3 FN), and HW-TIG (3.5 FN), its morphology and also the creep cavity density during creep deformation. The HW-TIG weld joint possessed significantly lower creep rupture life than that of the A-TIG and HLM weld joints. The HLM joint has exhibited a better creep rupture life than the A-TIG and HW-TIG weld joints. The microstructural constituents, *i.e.*, δ -ferrite content, columnar and equiaxed dendrites, and sigma (σ)-phase formation during creep, have significantly influenced the creep deformation and rupture strength of the joints. The orientation of the columnar structure, which is parallel to stress direction and lower δ -ferrite content in the A-TIG and HLM joints, has resulted in lower creep cavitation and higher creep rupture strength as compared to that of the HW-TIG weld joint. As the 316LN stainless steel weld joint processed by the HLM welding process exhibited the best creep rupture life, the HLM welding process is recommended for the welding of 316LN stainless steel.

<https://doi.org/10.1007/s11661-023-07208-4>

© The Minerals, Metals & Materials Society and ASM International 2023

I. INTRODUCTION

TYPE 316LN austenitic stainless steel is widely used in structural components of sodium-cooled fast reactors (SFRs) operating at high temperatures (from 823 K to 923 K). There is a significant desire to extend the design life from the existing level of 40 years to at least 60 years in order to improve the economic competitiveness of SFRs.^[1] The influence of nitrogen at concentrations greater than 0.08 wt pct on the high-temperature

mechanical behavior of type 316L stainless steel is being thoroughly explored as part of the design attempts to create structural materials suited for long lives. The addition of nitrogen provides benefits as a corrosion inhibitor, solid solution strengthener, and austenite stabilizer. In addition to increasing fracture toughness at cryogenic temperatures, nitrogen has also been demonstrated to improve creep and fatigue strength at elevated temperatures. Fusion welding has become an essential technique, particularly in the fabrication of SFR components. The conventional welding techniques, namely, tungsten inert gas (TIG), shielded metal arc (SMA), and metal inert gas (MIG) welding methods, have been commonly used for the fabrication of the components.^[2,3] Weld joints have an inhomogeneous microstructure compared to the base metal.^[4] Moreover, the fabrication of thick components necessitates multi-pass welding, which eventually introduces additional inhomogeneity into the fusion zone microstructure. In addition, hot cracking during the welding of austenitic stainless steel is a major problem in the fabrication process. To reduce hot cracking, the chemical composition of the base material and welding consumable is adjusted in such a way that the resulting fusion zone microstructure includes 3 to 10 pct delta (δ)-ferrite.

A.R. PAVAN and M. VASUDEVAN are with the Materials Development and Technology Group, Indira Gandhi Centre for Atomic Research, Kalpakkam, Tamil Nadu 603102, India and also with the Homi Bhabha National Institute, Training School Complex, Anushakthinagar, Mumbai 400 094, India. T. SAKTHIVEL and B. ARIVAZHAGAN are with the Materials Development and Technology Group, Indira Gandhi Centre for Atomic Research. Contact e-mail: arivu@igcar.gov.in. B.R. VAISHNAVI KRUPA is with the Materials Characterization & Engineering Group, Indira Gandhi Centre for Atomic Research, Kalpakkam, Tamil Nadu 603102, India and also with the Homi Bhabha National Institute.

Manuscript submitted May 11, 2023; accepted September 13, 2023.

Article published online September 29, 2023

However, the ferrite phase is highly unstable at elevated temperatures and acts as a potential site for the precipitation of intermetallic compounds in the material. It is demonstrated that, as the δ -ferrite content increases, the creep rupture life is reduced.^[5] This is due to the fact that a microstructure is more prone to creep cavitation as a result of the high amount of δ -ferrite in austenite matrix. The rupture life of the weld joint is reduced as ferrite number (FN) increases because more continuous δ -ferrite offers less resistance to creep crack propagation. The δ -ferrite content of a minimum of 5 vol pct is ideal for avoiding hot cracking as well as creep cavitation.^[6] Therefore, the volume fraction of ferrite in the weld joints, as well as its morphology associated with the welding process, also significantly affects creep properties.^[7,8] In order to circumvent this limitation and to improve the process capabilities such as productivity, penetration capability, and decrease the cost of thick joint preparation, advanced welding processes have been introduced. Therefore, with modified welding process conditions, the δ -ferrite content and proportion of the fusion zone area can be minimized to a lower extent in order to achieve improved creep strength.

The modified TIG welding processes known as hot wire TIG (HW-TIG) and activated-TIG (A-TIG) reduce the number of welding passes, welding cost, and production time.^[9,10] The 316LN weld joint fabricated by the A-TIG welding process has improved creep rupture strength as compared to conventional TIG weld joints.^[3,11] The improved creep rupture strength was attributed to lower δ -ferrite content, alignment of columnar grains along the loading direction, and less strength discrepancy between columnar and equiaxed structures. The high power density processes, namely, laser and electron beam welding, showed potential for the fabrication of austenitic stainless steels with a very narrow fusion zone.

Nevertheless, the thick weld joints can be fabricated using high density welding processes that significantly reduce welding heat input to fabricate a thick joint as compared to conventional arc welding techniques.^[12] However, to obtain a full penetration in thick (greater than 10 mm) 316LN plates, using laser and electron beam welding process requires very high power capacity, stringent process conditions, the necessity of a stringent straight butt configuration due to smaller spot size, the tendency to hot cracking due to large thermal gradient, the need of vacuum environment limits the use of these processes.^[13,14] The hybrid laser metal inert gas (HLM) welding technique was looked at as a viable method to fabricate the weld joints, which involves very few thermal cycles and at a higher welding speed in order to circumvent the aforementioned limitations. Arc and laser heat sources are used in the HLM welding technique to enhance fit-up tolerance and reduce temperature gradient, making it suitable for joining thick components. In addition, the HLM technique is preferred over autogenous laser welding because of its ability to modify the fusion zone microstructure by choosing the appropriate filler wire chemical composition.^[15]

In the present investigation, the creep deformation and rupture behavior of stainless steel 316LN weld joints fabricated from HW-TIG, A-TIG, and HLM welding processes have been systematically studied at 923 K. The hardness and microstructural investigations were performed in different conditions of the weld joints was reported.

II. EXPERIMENTAL

Type 316 LN stainless steel plates (dimensions: $250 \times 100 \times 11$ mm³) were joined using hot wire tungsten inert gas (HW-TIG), activated-tungsten inert gas (A-TIG), and hybrid laser metal inert gas (HLM) welding processes. The joint configuration for different welding processes is shown in Figure 1. The welding process parameters are given in Table I. The A-TIG and HW-TIG welding processes were carried out by using the Kuka make robotic welding setup. The A-TIG weld joint was produced using optimized welding parameters to achieve narrow weld zone in a single pass autogenously (without the use of external filler material).^[16] The HLM system included a laser and MIG welding system that used a Rofin slab CO₂ laser with a maximum power of 3.5 kW and proMIG 530 welding. The laser beam was operated in Gaussian mode (wavelength 10.6 μ m). A spot diameter of 180 μ m was achieved by using a 300 mm focal length. The macrographs of the fabricated weld joints are shown in Figures 2(a) through (f).

According to standard specifications (ASME section V article 2), an X-ray radiography examination was performed to qualify the weld joint. The chemical composition of the as-received base material and welds were analyzed using optical emission spectroscopy, which is listed in Table II. Residual stress measurements were carried out by X-ray diffraction technique using a portable residual stress measurement system (Proto iXRD) equipped with a manganese target ($K\alpha$, $\lambda = 2.10314$ Å).^[17,18] Wire-cut electrical discharge machining was used to fabricate the cross-weld creep specimens according to the dimensions, as shown in Figure 2(g). The gage length of the creep specimen comprises a fusion zone, HAZ, and base metal regions, as shown in Figure 2(g). Constant load creep experiments have been performed as per ASTM E139 in the air at 923 K in the stress range of 140 to 260 MPa. Test temperature was maintained within ± 2 K. A four-rod type extensometer attached with a digimatic digital indicator was used to continually record the specimen's elongation with a measurement accuracy of ± 0.001 mm. The δ -ferrite content was measured on the weld joints before and after creep tests using a feriscope (FMP30). The metallography samples were polished using a conventional technique up to 1 μ m and subsequently electrochemically etched using 10 pct oxalic acid solution to reveal the microstructure. The optical microstructure examinations were conducted using an inverted optical microscope (Zeiss Axio Observer 7 model). Further microstructural characterization was carried out using scanning electron microscopy (SEM)

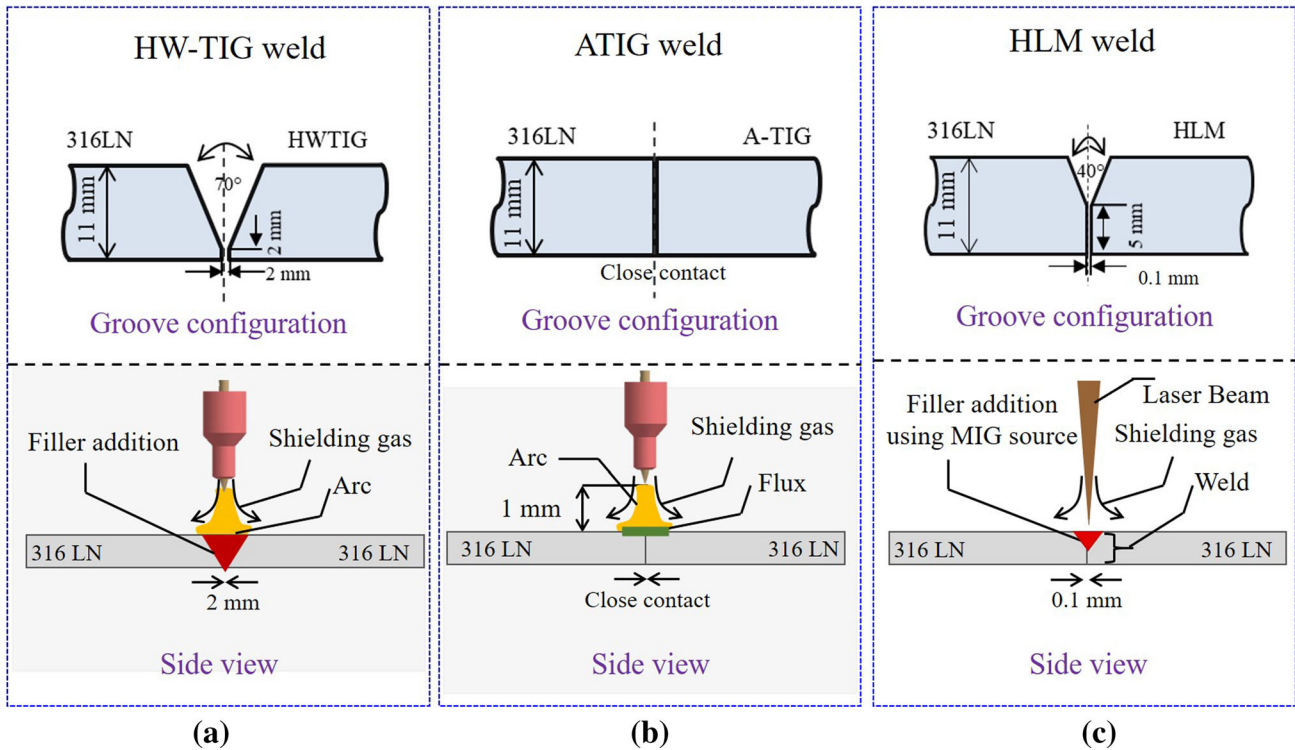


Fig. 1—The schematic representation of weld groove configurations used in (a) HW-TIG, (b) A-TIG, and (c) HLM welding processes.

Table I. Welding Parameters for Joining of 316LN Stainless Steel

Parameters	A-TIG	HW-TIG	HLM
Voltage (V)	14	10 (Avg)	23
Current (A)	270	126 (Avg)	120
Travel Speed (mm/s)	1	1.05 (Avg)	15
Laser Power (kW)	—	—	3.5
Shielding Gas (pct)	70 pct Ar + 30 pct He	pure Ar	pure He
Average Heat Input (kJ/mm)	2.7	0.9	0.38
Wire Feed Rate (mm/s)	—	3–11	66–108
Hot Wire Current (A)	—	15	—
Number of Passes	1	9	2
Defocusing Value (mm)	—	—	– 7
Laser–MIG Distance (mm)	—	—	2–3
Stick Out Length (mm)	—	—	17
Filler Wire Diameter (mm)	—	1.2	1.2
Laser Torch Angle	—	—	90 deg
TIG/MIG torch angle	90 deg	90 deg	60 deg

with energy-dispersive X-ray spectroscopy (EDS), and electron backscatter diffraction (EBSD). The SEM (Zeiss Sigma 300 machine) coupled with EBSD Model—Cswift detector (Make: Oxford Instruments). An accelerating voltage of 20 kV was used during EDS and EBSD scans. The specimen tilt at 70 deg and a working distance of approximately 10 mm to the specimen were used during the EBSD acquisition. All the EBSD patterns were collected at a magnification of 500 times (over an area of $200 \mu\text{m} \times 100 \mu\text{m}$) and a step size of $0.15 \mu\text{m}$. The Kikuchi patterns (~ 8 to 10 numbers) were collected to index fcc (matrix austenite), bcc [δ] ferrite, and tetragonal [σ] (transformed δ -ferrite) phases. The acquired EBSD data were

processed using HKL® channel-5 software. The kernel average misorientation (KAM) is calculated to reveal the distribution of strains using a 5×5 kernel with a higher misorientation angle taken as 5 deg.

III. RESULTS AND DISCUSSION

A. Microstructure

The microstructure of type 316LN austenitic stainless steel is shown in Figures 3(a) and (d). The as-received base material average grain size is around $39 \mu\text{m}$. The SEM-secondary electron (SE) micrographs and EBSD

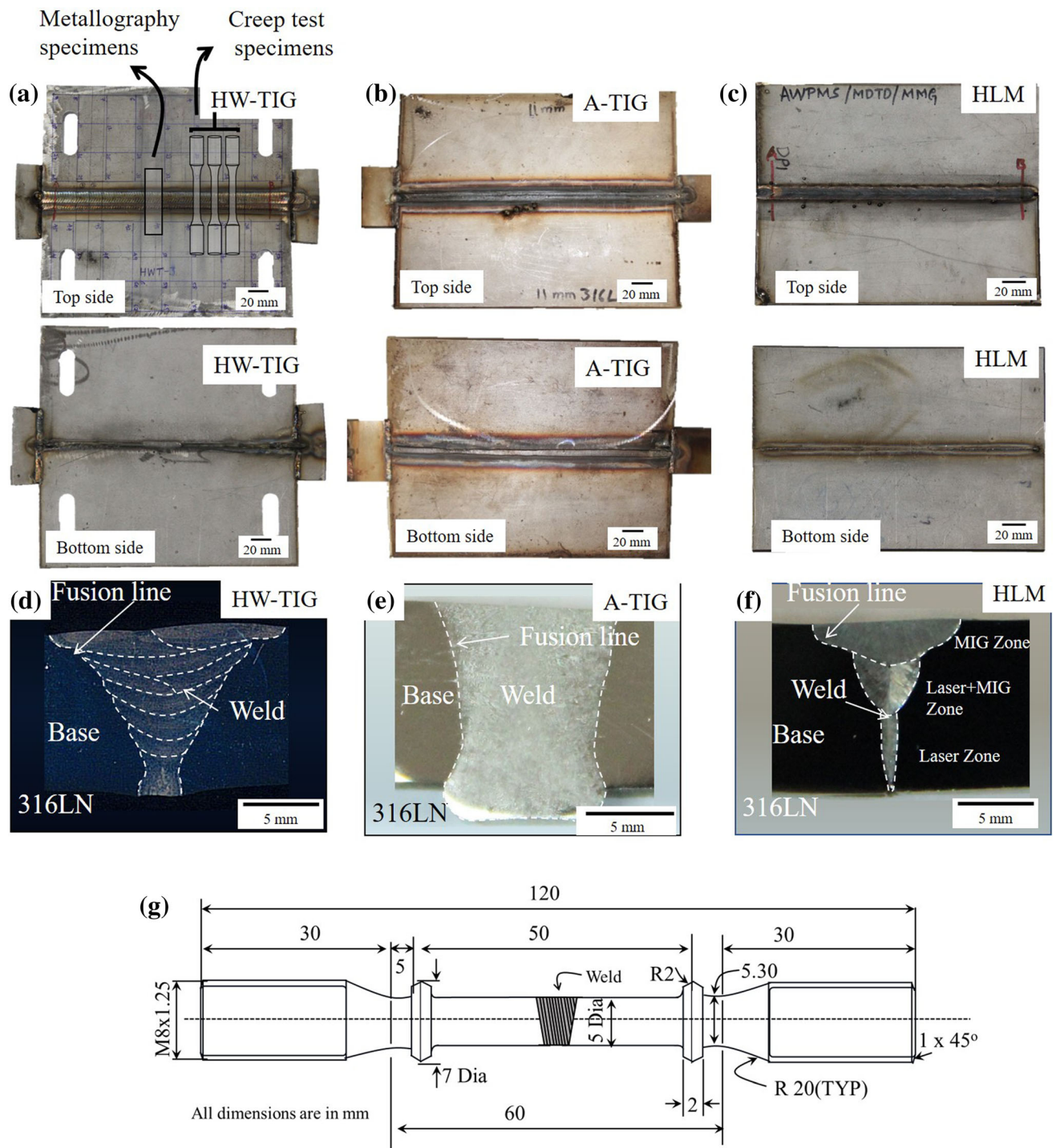


Fig. 2—Photographs showing the (a) HW-TIG, (b) A-TIG, and (c) HLM weld joints and corresponding macrographs in (d), (e), and (f), respectively, and also the positions from which the metallography and creep test specimens were extracted. The schematic of the creep specimen dimension is shown in (g).

phase map confirm the presence of δ -ferrite (less than 0.02 pct) stringers in the as-received base material [Figures 3(c) and (d)]. The microstructure of the weld joints in the as-weld condition is shown in Figure 4. The A-TIG weld metal microstructure consists of equiaxed dendrites surrounded by columnar dendrites with δ -ferrite in the interdendritic regions that solidified in

primary austenite–ferrite (AF) mode. In contrast, the HW-TIG weld metal exhibited mixture of skeletal, lathy, and globular ferrite morphology. This type of ferrite morphology is typically seen during the primary ferrite to austenite (FA) mode of solidification, with the retained ferrite at the core of the dendrites. Similar to HW-TIG weld joint, skeletal ferrite was observed in the

Table II. Chemical Composition of Base and Weld Metals (Wt Pct)

Materials	Fe	Cr	Ni	Mo	Mn	Si	C	S	P	N
Base Metal	bal.	16.80	12.03	2.45	1.68	0.47	0.029	0.001	0.02	0.10
A-TIG Weld	bal.	16.88	12.21	2.32	1.67	0.48	0.029	0.001	0.02	0.08
HLM Weld	bal.	17.26	11.81	2.34	1.70	0.68	0.021	0.001	0.02	0.06
HW-TIG Weld	bal.	18.23	12.22	2.11	1.71	0.47	0.017	0.001	0.01	0.05
316L Filler	bal.	18.22	11.14	2.75	1.80	0.85	0.01	0.001	0.01	—

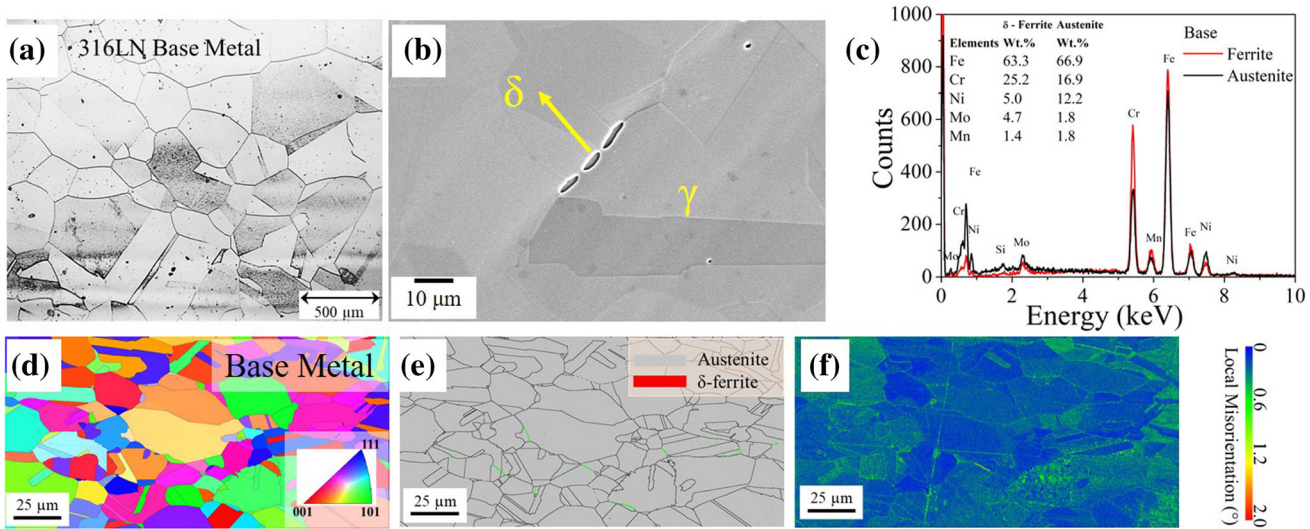


Fig. 3—(a) Optical and (b) SE micrograph of Type 316LN stainless steel microstructure with (c) point EDS elemental analysis showing the compositional variations on austenite matrix and ferrite, (d) through (f) presents the EBSD images, phase maps, and strain distribution maps obtained for 316LN base material.

capping pas (MIG influenced zone) of HLM weld joints, while the laser + MIG and laser-influenced zones of HLM weld exhibited columnar and equiaxed dendrites, respectively. The difference in ferrite morphology at various zones is attributed to the filler material addition.

The microstructural morphology difference can be attributed to the change in the ratio of chromium equivalent (Cr_{eq}) and nickel equivalent (Ni_{eq}) (Table III) and also weld cooling rate.^[19] Moreover, the epitaxial type growth of columnar dendrites was oriented transverse to the welding direction due to temperature gradient in the A-TIG weld metal, whereas in HLM and HW-TIG weld metals, the directional orientation of the dendrites was relatively lower than in A-TIG weld metal due to the multiple number of passes.

Furthermore, the EDS analysis reveals the compositional variation in δ -ferrite and austenite of all the welds, as shown in Figure 5. The δ -ferrite significantly affects the creep rupture life of the weld joints. A weld metal is more susceptible to creep cavitation damage during creep testing if it has high δ -ferrite content.^[7,21] Therefore, variations in δ -ferrite content across the HW-TIG, A-TIG, and HLM weld joints were mapped (Figure 6). However, the ferrite content is preferred in the range of 3 to 7 FN to prevent hot cracking in 316LN weld joints, and therefore, it cannot be avoided in

austenitic stainless steel weld joints.^[7,22] It is evident from Figure 6 that the δ -ferrite content was relatively higher in HW-TIG weld metal as compared to A-TIG and HLM weld metals. It should be noted that the δ -ferrite was uniformly distributed in the A-TIG weld joint, while the HLM (capping pass) and HW-TIG weld joint displayed the higher and non-uniform distribution of δ -ferrite content (Figure 6). The higher δ -ferrite in HLM (capping pass) and HW-TIG can be attributed to the filler metal addition containing a higher amount of ferrite stabilizers such as chromium, molybdenum, and silicon. Nonetheless, the average δ -ferrite content in the HLM weld joint was lower than the A-TIG and HW-TIG weld joint owing to the relatively lower proportion of fusion zone area. Moreover, it should be noted that the average δ -ferrite content was relatively higher in HW-TIG weld metal (3.5 FN) compared to A-TIG (1.7 FN) and HLM (1.3 FN) weld metals.

The hardness variation across the HW-TIG, A-TIG, and HLM weld joints is shown in Figure 7. The hardness variation in the HW-TIG and HLM weld joints was relatively higher than the A-TIG weld joint. In addition, higher hardness across the joint was observed in the weld metal of HW-TIG and HLM joints compared to other regions. The heat-affected zone (HAZ) of HLM and HW-TIG has shown similar to

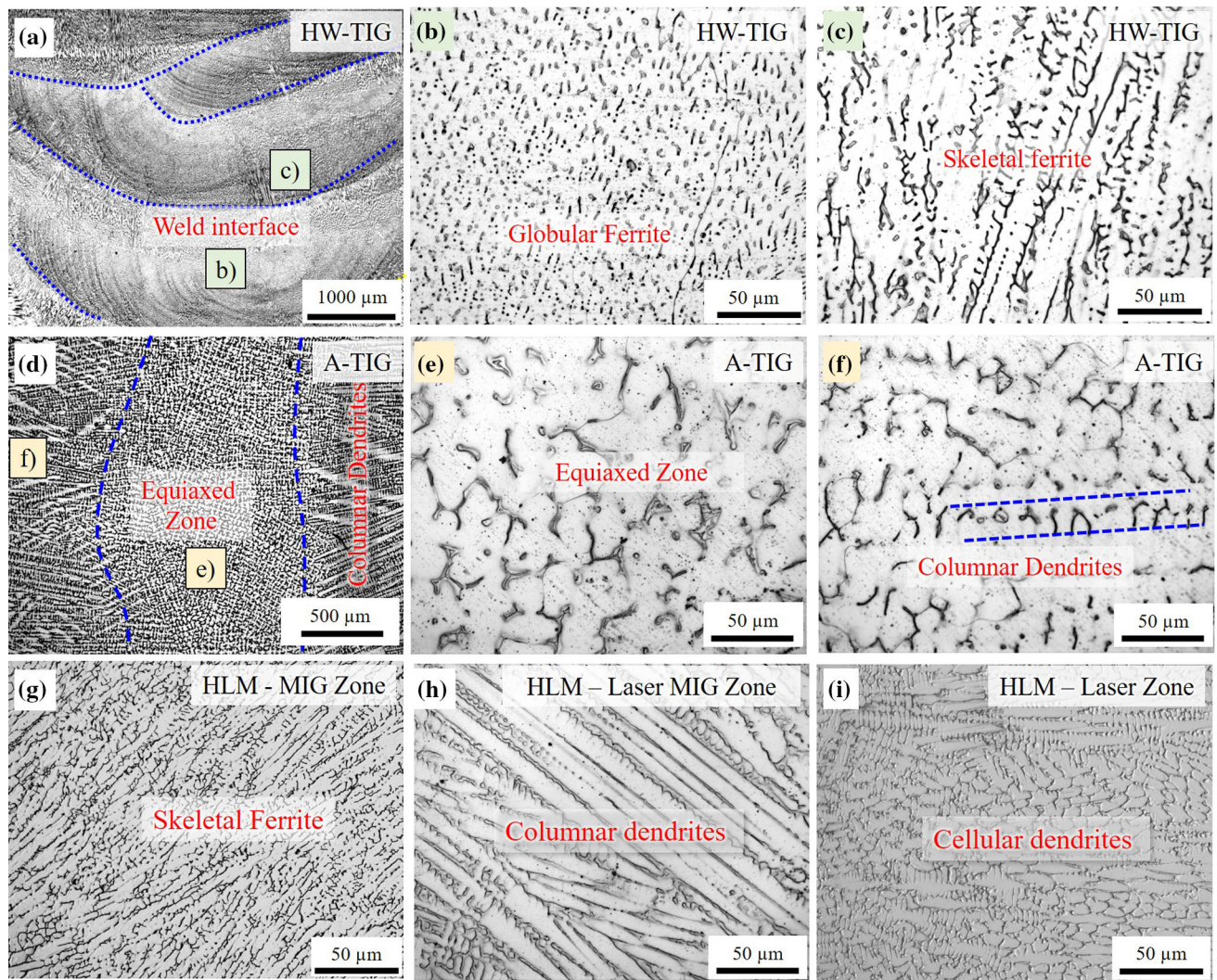


Fig. 4—Optical micrographs of (a through c) HW-TIG, (d through f) A-TIG, and (g through i) HLM weld joints exhibiting the microstructural variation in different zones.

Table III. Chromium (Cr_{eq}) and Nickel (Ni_{eq}) Equivalent Using Hammar and Svensson's Equivalency Formula^[20]

Material	Cr_{eq}	Ni_{eq}	Cr_{eq}/Ni_{eq}
HW-TIG Weld Metal	21.82	13.83	1.577
A-TIG Weld Metal	20.78	14.57	1.426
HLM Weld Metal	21.63	13.65	1.584

weld metal hardness (~ 200 to 210 $VHN_{0.3}$). The hardness of the weld metal and HAZ in the HLM and HW-TIG weld joints (~ 200 to 210 $VHN_{0.3}$) was higher than the base metal (~ 160 to 180 $VHN_{0.3}$) region. However, A-TIG weld metal has exhibited lower hardness (~ 145 $VHN_{0.3}$). The higher hardness in the HAZ of HLM and HW-TIG weld joints was due to higher strain accumulation caused by the multiple thermal cycles during welding than the A-TIG weld joint.^[23] In addition, it can be attributed to the higher transverse

residual stress (Figure 7(c)). The evolution of residual stress during the welding process significantly depends on the material properties (yield strength, thermal expansion coefficient) and constraints.^[17] The study conscientiously demonstrated the constraint effect on the magnitude of residual stress and showed that transverse residual stress builds up more during multiple depositions (filling the groove) than that of longitudinal residual stress (Figure 7(b)).^[17] Therefore, higher hardness in the base material of HW-TIG weld joint could be due to the presence of higher transverse residual stress. It can be noted that the hardness variation was uniform in A-TIG weld metal due to homogeneous microstructure (Figure 6(b)) with uniform variation of transverse residual stress (Figure 7(c)). The lower transverse residual stress and its uniform distribution are attributed to the straight-sided butt joint configuration. This configuration was welded using a single-pass autogenous technique, which eventually minimized the shrinkage strains.^[18,24] Therefore, the combined influence of higher δ -ferrite content, residual stress, and strain

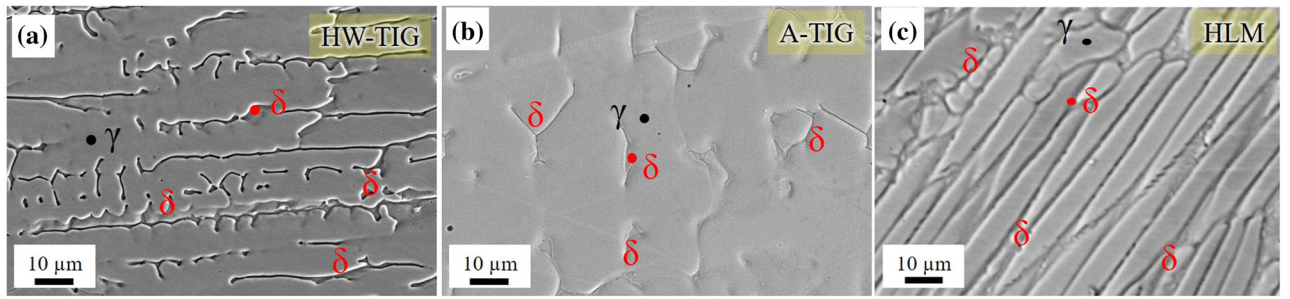


Fig. 5—SE micrographs of (a) HW-TIG, (b) A-TIG, and (c) HLM weld joints with EDS elemental analysis.

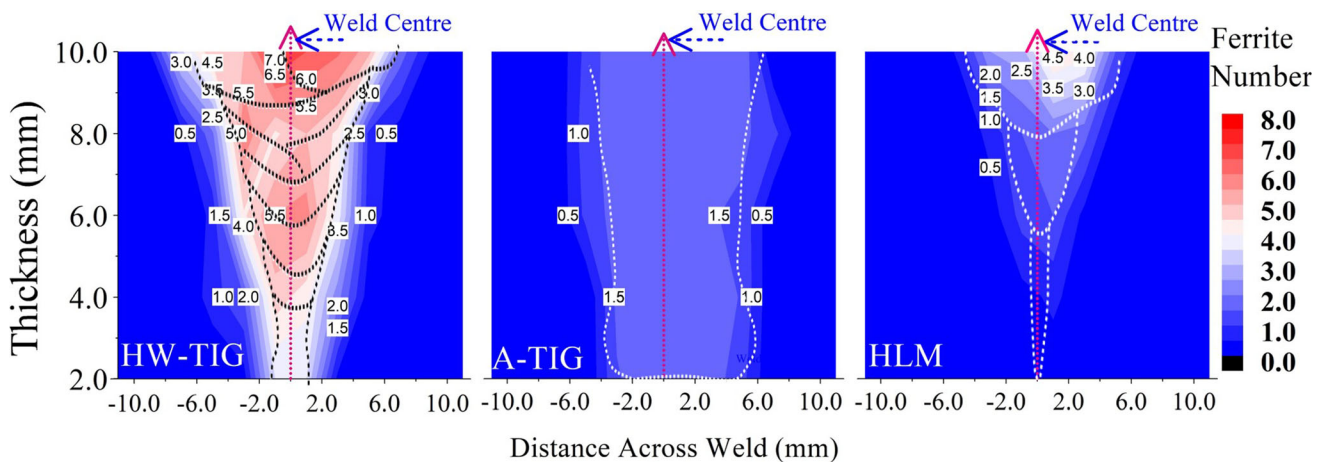


Fig. 6—Contour map of δ -ferrite content in weld joints.

hardening caused during multiple thermal cycles (deposition of filler material during subsequent passes) resulted in higher hardness in the HLM and HW-TIG fusion zones as compared to A-TIG. Also, the variation in hardness within the weld metal can be attributed to the strain hardening, heterogeneous distribution of δ -ferrite content (harder phase than the austenite), and a mixture of columnar and equiaxed dendrites.^[20,25,26]

B. Creep Deformation Behavior of 316LN Stainless Steel Weld Joints

Uniaxial creep tests were conducted in ambient air at 923 K under various applied stress 140, 160, 180, 200, 220, and 240 MPa. The creep curves of 316LN stainless

steel weld joints fabricated by HW-TIG, A-TIG, and HLM welding processes are presented in Figure 8. The creep curves clearly display the typical three regimes, namely primary, secondary, and accelerating tertiary creep. The reduction in applied stress has resulted in longer creep times with a lower creep rate in all the weld joints. HLM weld joint has experienced longer creep exposure as compared to HW-TIG and A-TIG under similar testing conditions. In addition, the A-TIG weld joint has experienced longer creep exposure than the HW-TIG weld joint. The creep strain accumulation was higher in the HLM and A-TIG weld joints than the HW-TIG weld joint (Figure 9). The results clearly show the significant enhancement in creep strength of the 316LN stainless steel weld joint fabricated by the HLM process in comparison with that of other two processes.

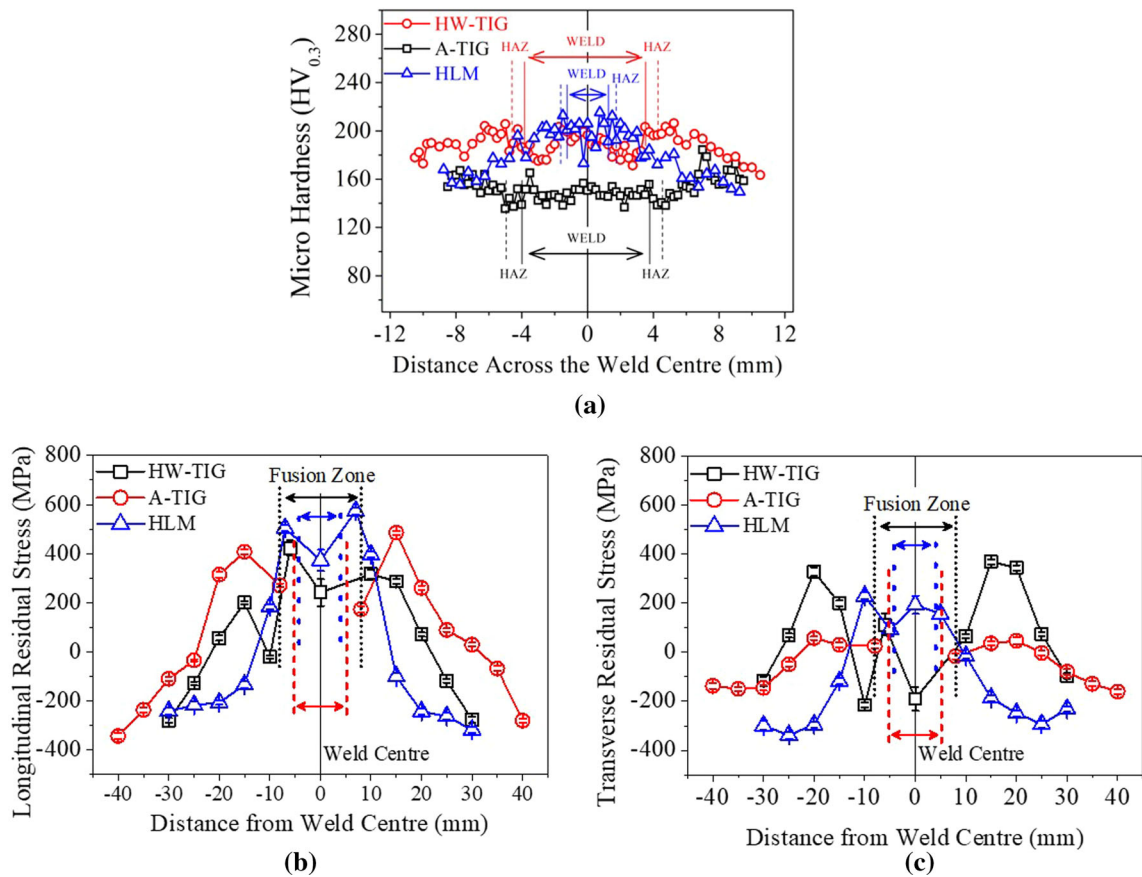


Fig. 7—Variation of (a) micro-hardness, (b) longitudinal, and (c) transverse residual stress across the weld joint.

The variation in creep rate with time (logarithmic scale) for the weld joints over the stress range of 140 to 240 MPa is shown in Figure 10. The creep rate decreased as the applied stress reduced, and the onset of tertiary creep was delayed in all the cases. Notably, in the primary creep regime, the creep rate was attributed to the localized deformation and strain accumulation.^[27] Notably, the significant variation in microstructural constituents observed in HW-TIG weld joints limits the local deformation and eventually leads to the early onset of tertiary creep.

The creep rate was similar in all the weld joints in the respective stress levels, as shown in Figure 11. However, the onset of the tertiary creep regime was found to vary. This variation in creep properties can be attributed to the variation in microstructure and δ -ferrite content in the respective weld joints. The delay in the tertiary regime is in the following order: HW-TIG < A-TIG < HLM, and it exhibited a good correlation with the order of δ -ferrite content present in the weld joints. Multiple thermal cycles and higher ferrite content in the HW-TIG weld joint limit the deformation, causing the early commencement of tertiary creep.

The variation of minimum creep rate under different stress levels of HW-TIG, A-TIG, and HLM weld joints at 923 K is depicted in Figure 12. The steady-state creep rate ($\dot{\epsilon}_{\min}$) variation as a function of applied stress (σ) was found to obey Norton's power law of creep

($\dot{\epsilon}_{\min} = A \times \sigma^n$), where n is the stress exponent, and A is a constant. The n values were found to vary in the range of 10.3 to 11.3. These stress exponent values imply that dislocation creep is the rate-controlling mechanism in all of these cases. The observed stress exponent values were comparable to the literature-reported values.^[28]

The weld joints experienced a higher rate of deformation and lower creep rupture life as compared to the base metal. Among the weld joints, the HW-TIG weld joint possessed a lower creep rupture life than the A-TIG and HLM weld joints. The loss of creep rupture strength of the HW-TIG weld joint is significantly higher with a decrease in applied stress. In comparison, the HLM joint has exhibited a relatively higher rupture life than the A-TIG weld joint. The microstructural constituents, *i.e.*, δ -ferrite, columnar and equiaxed dendrites, and σ -phase formation during creep substantially influenced the creep deformation and rupture strength of the joints. The base metal demonstrated higher creep rupture life compared to all weld joints. Among the weld joints, the HLM joint showed relatively better creep rupture strength compared to all other weld joints, as shown in Figure 13. The orientation of the columnar structure, which is parallel to stress direction and lower δ -ferrite content in the A-TIG and HLM joints, resulted in higher creep strength as compared to that of the HW-TIG weld joint. It should be noted that all the weld joints exhibited higher creep strength than

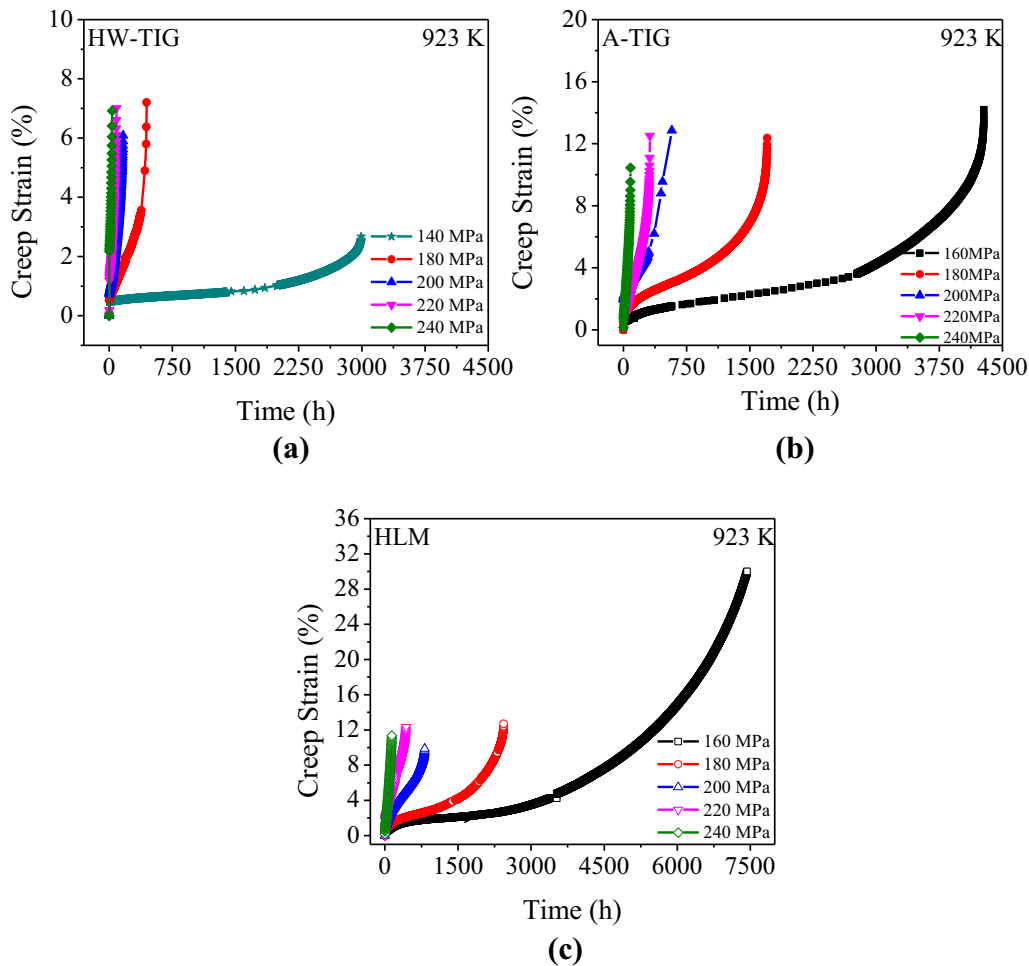


Fig. 8—Variation of creep strain with time of 316LN weld joints at (a) HW-TIG, (b) A-TIG, and (c) HLM weld joints at 923 K and over the stress range of 140 to 240 MPa.

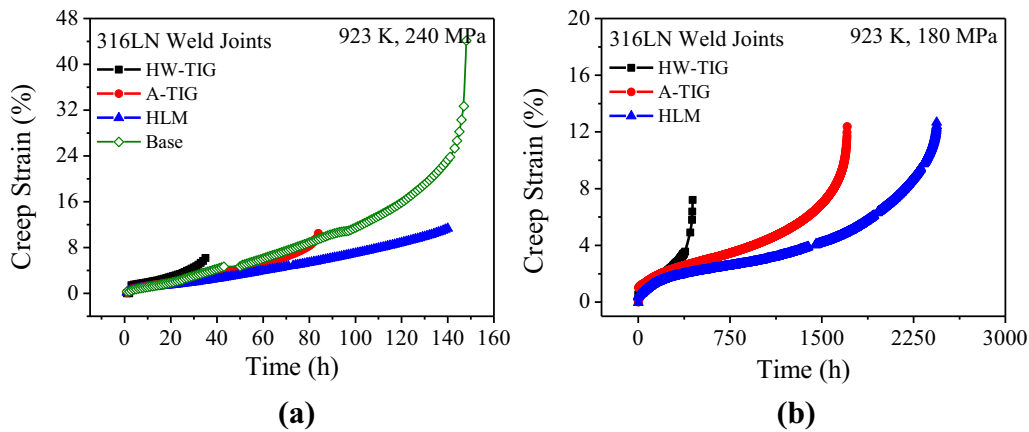


Fig. 9—Comparison of creep curves of 316LN weld joints at (a) 923 K, 240 MPa and (b) 923 K, 180 MPa.

the recommended Recueil de Règles de Conception et de Construction (RCC-MR) data (design and construction rules for mechanical components).^[29] The RCC-MR code comprehensively outlines the methods to fulfill primarily the basic requirements pertaining to the design, construction, starting, operation, maintenance,

and in-service inspection demands. This code defines that safety can be ensured solely through the quality of manufacturing and design.^[29]

The stability of the δ -ferrite in the weld metal substantially impacts the ductility of austenitic stainless steel weld metal. Since δ -ferrite is a metastable phase, it

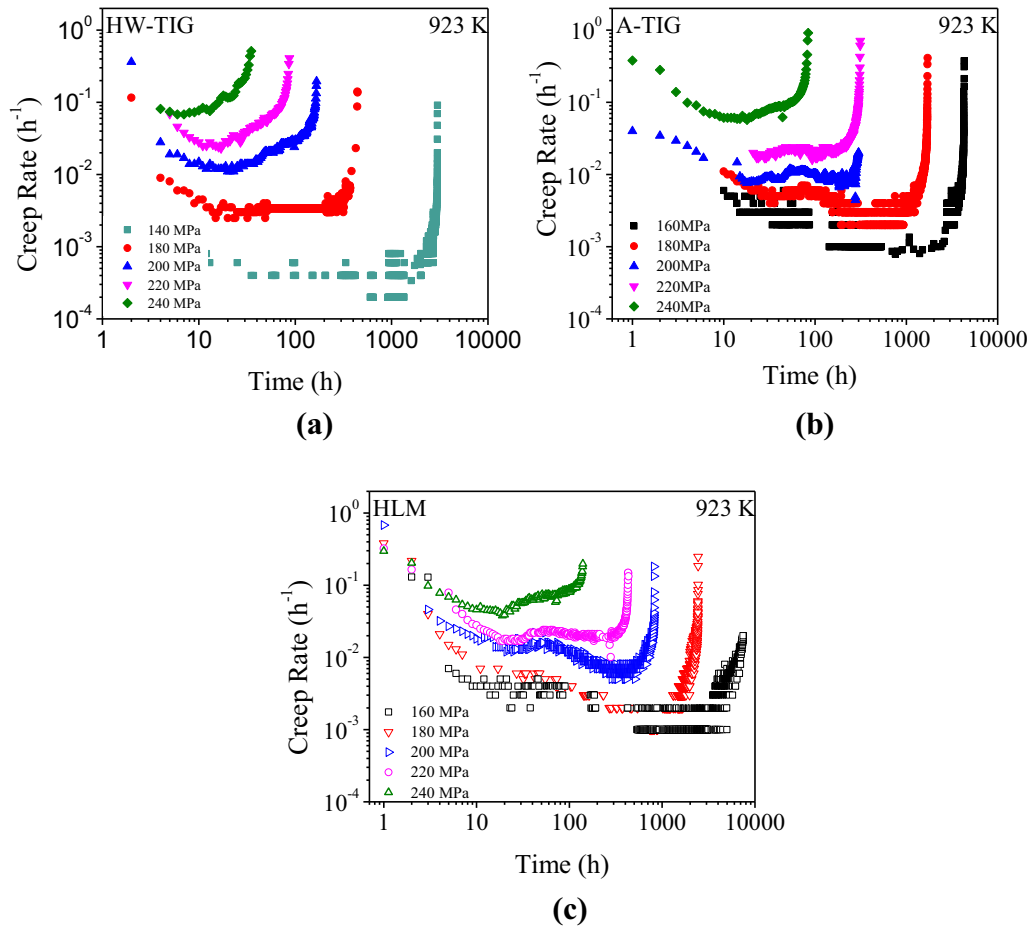


Fig. 10—Variation of creep rate with time of 316LN weld joints at (a) HW-TIG, (b) A-TIG, and (c) HLM weld joints at 923 K and over the stress range of 140 to 240 MPa.

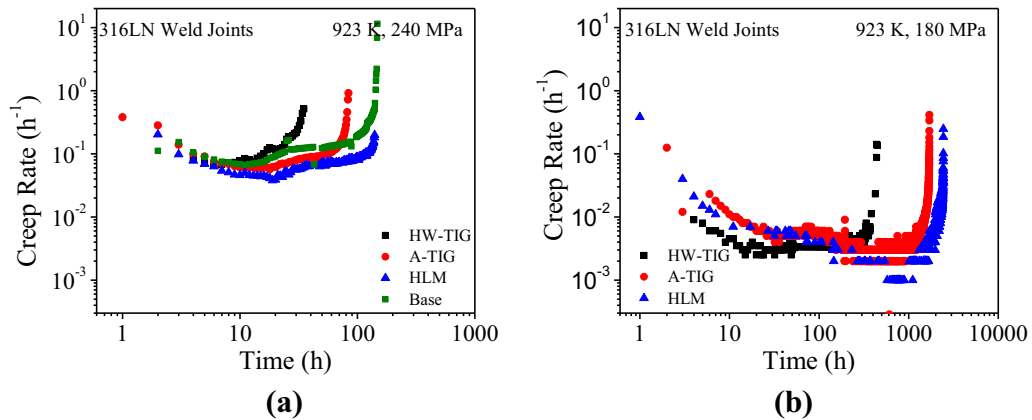


Fig. 11—Comparison of creep rate with time of 316LN weld joints at (a) 923 K, 240 MPa and (b) 923 K, 180 MPa.

will undergo phase transformation under thermal exposure. Figure 14 illustrates the elongation (pct) and reduction area (pct) variation with rupture life. The HW-TIG weld joint showed the least ductility compared to other joints. It should be noted that all the weld joints exhibited lower ductility than that of base material (Figure 15). In weld joints, the ruptured specimens clearly display substantial localized deformation in the

weld joints. Moreover, A-TIG and HLM weld joints displayed good ductility among the weld joints. This can be ascribed to various factors like inhomogeneous microstructure associated with multiple thermal cycles, orientation of grains, ferrite content in the fusion zone, and weld constraint effect. At prolonged creep exposure, the precipitates coarsen, and the ferrite transforms into brittle intermetallic compounds that eventually act as

cavity nucleating sites.^[30] Consequently, weld joints exhibited relatively lower ductility and creep rupture life than the base material. In addition to these factors, the sharp change in the microstructure of weld joints, from

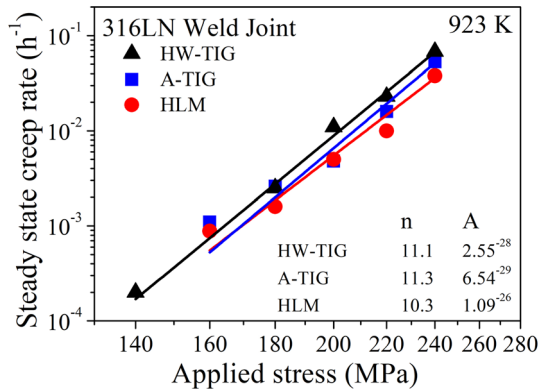


Fig. 12—Comparison of steady-state creep rate as a function of applied stress of base metal, HW-TIG, A-TIG, and HLM weld joints.

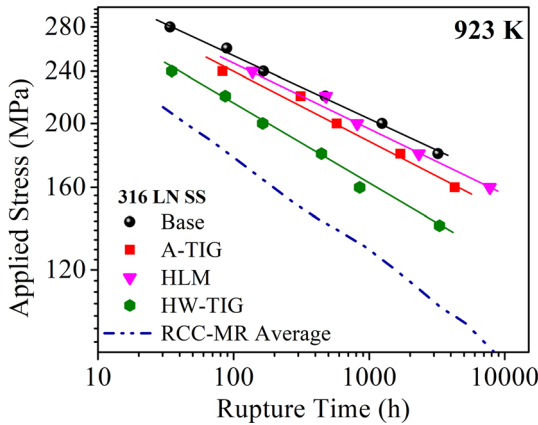


Fig. 13—Comparison of creep rupture life curves as a function of applied stress of base metal, HW-TIG, A-TIG, and HLM weld joints and RCC-MR curve.

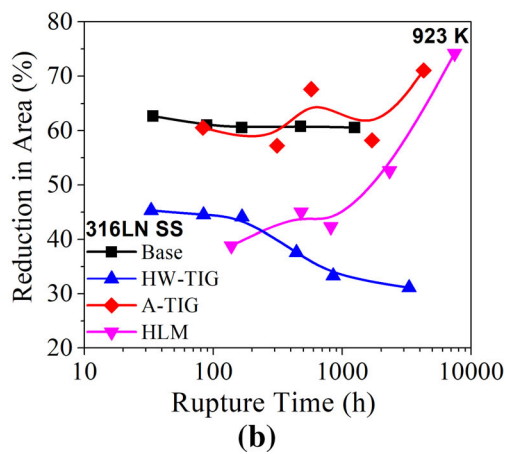
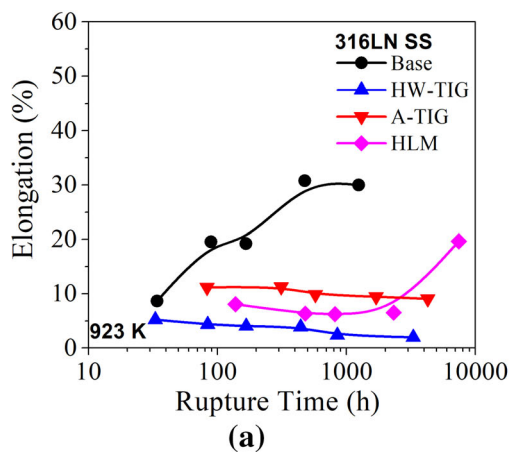


Fig. 14—(a) Variation of elongation (pct) and (b) reduction in area (pct) as a function of rupture life of base metal, HW-TIG, A-TIG, and HLM weld joints at 923 K.

base to HAZ to fusion zone, acts as a metallurgical notch that deteriorates the creep properties.

The fracture surface of the crept specimen revealed fine dimples in HW-TIG weld joints, while A-TIG and HLM weld joints exhibited relatively coarser dimples suggesting the ductile mode of failure (Figure 16). However, the more interconnected creep cavities associated with the intermetallic sigma phase in HW-TIG weld joint caused the relatively brittle type of inter-granular creep failure than that of A-TIG and HLM weld joints. As already seen earlier in Figure 11, the earlier onset of tertiary creep in HW-TIG and A-TIG weld joints compared to HLM weld joint indicates a faster rate of damage accumulation. The failure has occurred in the fusion zone of the weld joints in all the cases (Figure 17), suggesting the vulnerability of the inhomogeneous microstructure under creep exposure. The HW-TIG weld joints had more surface and interior cracks than the other two joints (Figure 17). This can be directly correlated to the amount of ferrite in the weld metal. It is evident that in the A-TIG weld joint, the columnar dendrites are parallel to the loading axis, while the equiaxed grains are perpendicular. Thus, the failure has occurred in the columnar–equiaxed zone interface. This could be because the equiaxed zone is relatively softer than the columnar grains.^[11]

The δ -ferrite is rich in ferrite-stabilizing elements such as Cr, Mo, and Si, and the diffusion of these elements is faster than in the austenite phase at elevated temperatures due to its body-centered cubic structure.^[31–33] This eventually leads to the formation of a brittle intermetallic phase called the sigma phase, which is possibly rich in 44 wt pct Fe, 29.2 wt pct Cr, 8.3 wt pct Mo having a tetragonal crystal structure.^[34,35] Figure 18 depicts the conversion of ferrite into other phases under creep and thermal exposure, indicating that almost 90 pct of the transformation has occurred during creep (~ 100 hours at 923 K), whereas the phase transformation was delayed in thermally exposed specimens (Figure 18(b)) when compared to creep-exposed specimens (Figure 18(a)). This suggests that the phase transformation rate is faster under applied stress (Figure 18).



Fig. 15—Creep ruptured specimens tested at 923 K depicting the fracture location with reduction in ductility.

Variation of hardness across the weld joint in creep and thermally exposed specimens tested at 923 K is shown in Figure 19. Higher hardness near the fracture end of A-TIG and HLM weld joints can be due to the presence of brittle intermetallic compound and dislocation density (Figure 19(a)). On the other hand, the reduced hardness near the fracture end of the HW-TIG weld is attributed to the higher creep cavities and cracks (Figure 19(b)). The hardness variation in thermally exposed specimens of short-time exposure (Figure 19(c)) and long-time exposure (Figure 19(d)) has been plotted. The hardness variation across the weld joint has been found to be decreased compared to the as-weld condition (Figure 7). This could be due to the relaxation of residual stresses. However, a higher magnitude of hardness can be ascribed to the precipitation of brittle intermetallic compounds.

In order to further understand the variation in microstructure and creep cavitation under creep exposure, creep-ruptured specimens were characterized using SEM. Figures 20 and 21 present the microstructural variations during creep exposure, while Figure 22 depicts the thermally exposed specimens (aged till the creep rupture time). The figures reveal the decomposition of the δ -ferrite network into the second phase particles which are rich in Fe, Cr, and Mo (Figure 23). During creep of 316LN weld joints, the degradation of δ -ferrite network occurs in following sequence, initially Cr_{23}C_6 carbides precipitate and then with the further creep exposure, the formation of intermetallic sigma

phase transformation takes place, subsequently coarsening of these undesired particles/carbides follows.^[7] It is known that nitrogen is a better solid solution strengthener compared to carbon and has been reported to delay the onset of carbide precipitation and to impede the coarsening of carbides. As a result, the possible presence of fine precipitates could improve the strength of 316LN stainless steel weld joints by arresting the grain boundary sliding and hindering the dislocation movement.^[7]

Further, the magnified SE micrographs presented in Figure 21 reveal the degradation and breaking of δ -ferrite into the brittle intermetallic compound. As said earlier, the ferrite content plays a predominant role in deciding the creep strength of the weld joints. During creep exposure, cavitation occurs at the interface of decomposed ferrite networks and austenite matrix.^[7,8,36] As time progresses, propagation of cavities takes place along the ferrite network and eventually leads to rupture. The nucleation of the creep cavity can be observed near the interface, which is associated with the brittle sigma phase (Figures 17 and 19). It should be noted that the ferrite content and its morphology are different in HW-TIG, A-TIG, and HLM weld joints. The HW-TIG weld joint consisted of both networked and discontinuous ferrite morphology with high ferrite content (2.5 to 7 FN), while the A-TIG and HLM weld joint consisted of ferrite morphology with lower ferrite content (A-TIG: 1.7 FN; and HLM: 0.2 to 4 FN). The transformation of δ -ferrite to sigma phase is evident

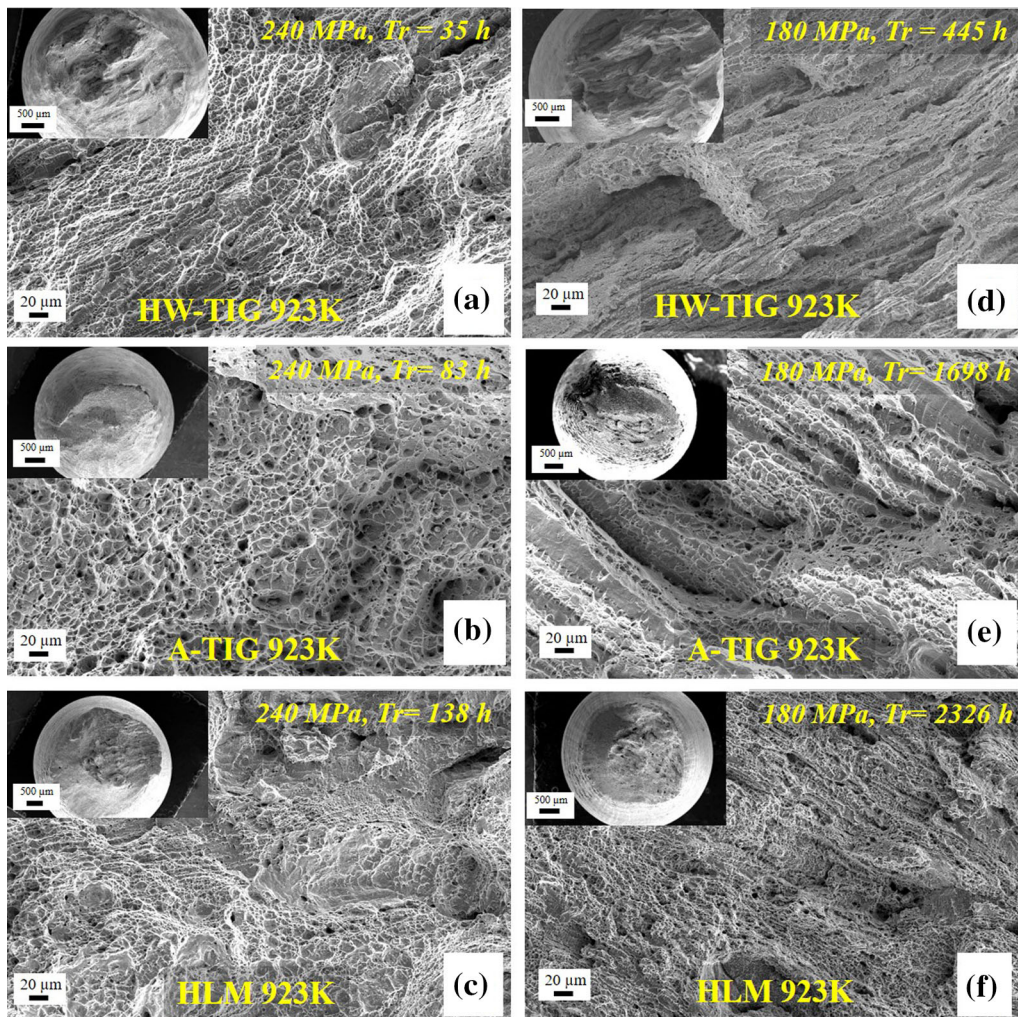


Fig. 16—Fracture surface of (a, d) HW-TIG, (b, e) A-TIG, and (c, f) HLM weld joints tested at 923 K.

from the phase map (Figure 24). Among the weld joints, HW-TIG weld showed higher δ -ferrite content (Figure 24(a)). Thus, higher creep cavitation was observed in the HW-TIG joint than in the other joints due to the presence of more brittle sigma particles at the interfaces.

It is understood from the earlier work^[11] that enhancement in creep rupture strength could be obtained by achieving lower δ -ferrite content, aligned columnar grains and δ -ferrite in the loading axis, and less strength discrepancy between columnar and equiaxed grains in austenitic stainless steel weld joints. The skeletal δ -ferrite morphology is more susceptible to cavitation than the globular ferrite. In addition, the heterogeneous variation in strength across the joint and within the weld metal (variation in dendrites size and orientation, δ -ferrite content, and morphology) leads to early nucleation of creep cavitation.^[37] Similar to these observations, as reported, the higher creep rupture life

of HLM and A-TIG weld joints can be attributed to the lower ferrite content and the alignment of grains along the loading axis. In addition, both A-TIG and HLM weld joints exhibited discontinuous ferrite, which is isolated and randomly distributed in the austenite matrix (Figures 4 and 5). On the other hand, HW-TIG weld joints displayed predominantly skeletal ferrite networks. Although the influence of globular ferrite on creep cavitation damage is relatively lower than the skeletal ferrite, the increased amount of globular ferrite (*i.e.*, the closer spatial distance between globular ferrite) leads to higher creep cavitation, which eventually resulted in reduced creep rupture strength.^[7,8,22] The present work used the combination of helium and argon shielding gases to improve the A-TIG welding arc characteristics, thereby reducing the proportion of fusion zone area.^[16] This has reduced the weld metal volume as well as δ -ferrite content in the fusion zone. Hence, this factor caused the improvement in the creep

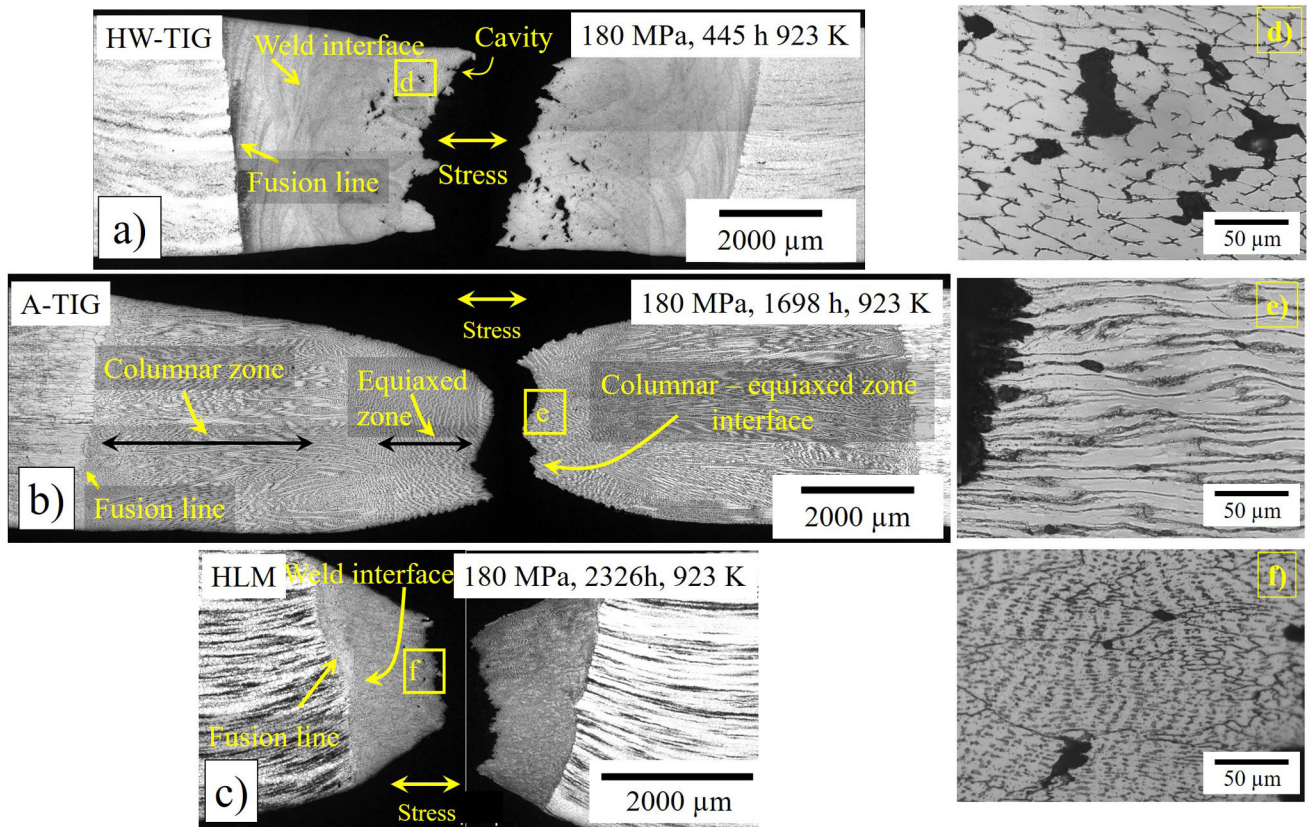


Fig. 17—Macrostructure of crept specimens indicating the location of failure in (a) HW-TIG, (b) A-TIG, and (c) HLM weld joints and corresponding microstructures near the fracture zone (d through f) tested at 923 K and 180 MPa.

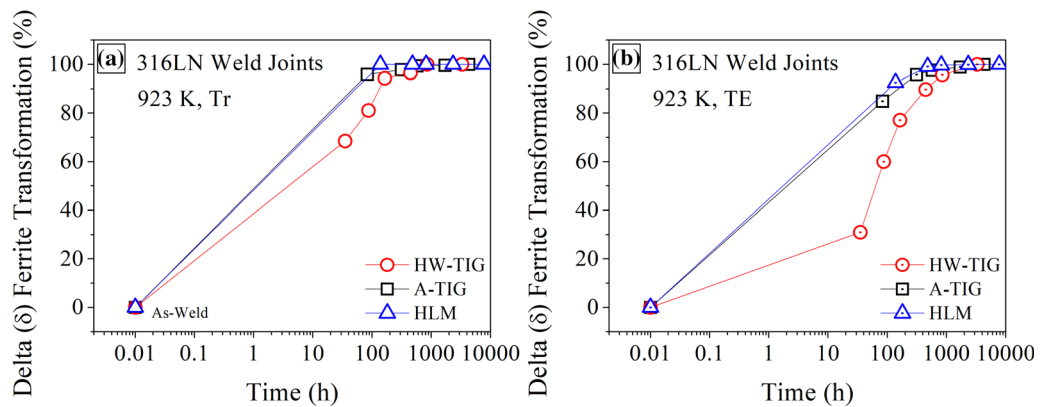


Fig. 18—Transformation of δ -ferrite in the fusion zones of HW-TIG, A-TIG, and HLM weld joints under (a) creep exposure (Tr) and (b) thermal exposure (TE) at 923 K.

rupture strength of the A-TIG weld joint (~ 35 pct) compared to the weld joint fabricated from a conventional TIG process.^[7,11,36]

The microstructural observations confirm the formation of the sigma phase in both creep and thermally exposed specimens of all the weld joints. It is also

revealed that creep cavities appear to be located with the Cr, Mo rich compounds. From the equilibrium phase diagrams of the weld joints, including base material, it is clear that in all the cases, the sigma phase formation temperature is below ~ 850 °C (1123 K), as shown in Figure 25. This indicates that during creep deformation

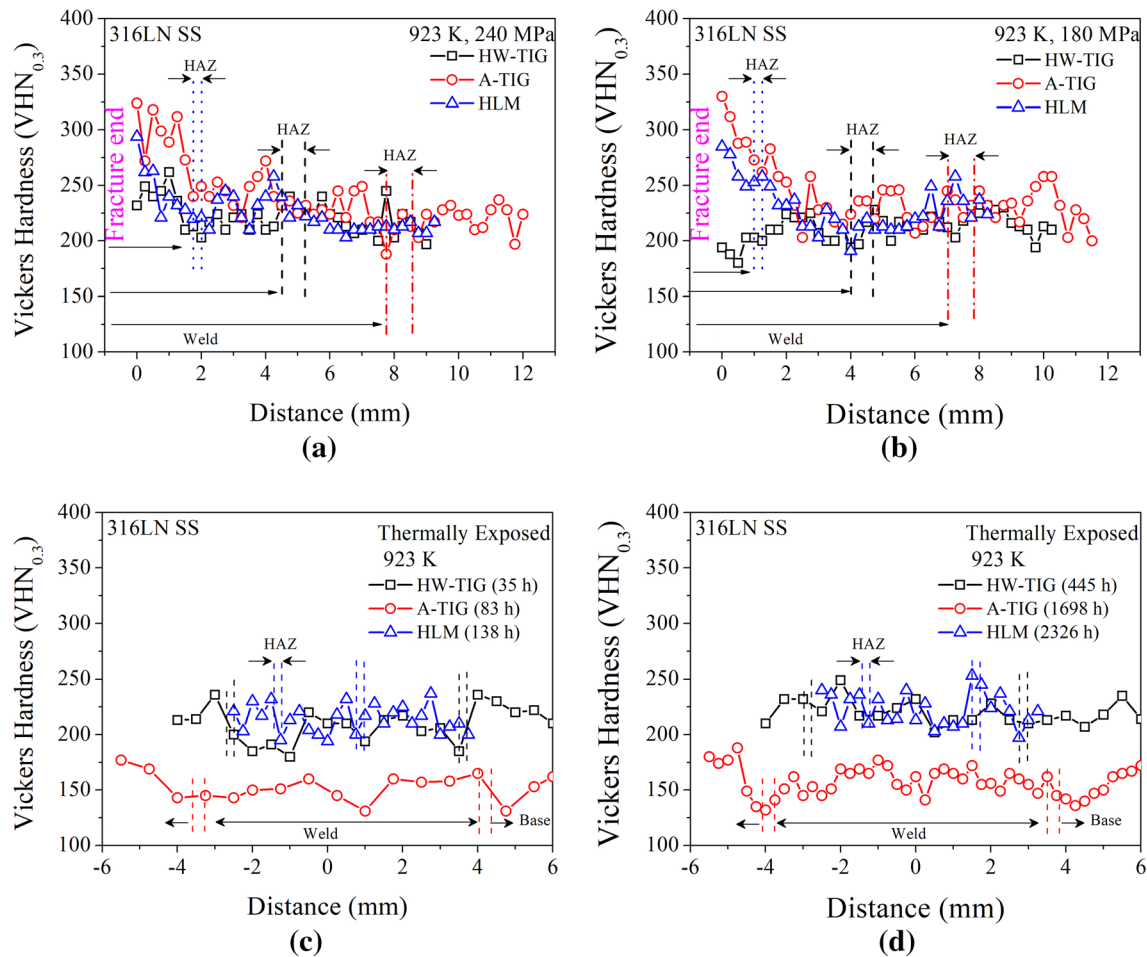


Fig. 19—Micro-hardness variation in creep-exposed specimens (a) 240 MPa, (b) 180 MPa, and (c, d) thermally exposed specimens at 923 K.

at 923 K, δ -ferrite in the fusion zone of all the weld joints experiences a significant level of thermodynamic driving force to the formation of intermetallic brittle sigma phase. Furthermore, the thermodynamic equilibrium calculations manifested low sigma phase volume fractions of 6.7, 14.9, 8.3, and 10.7 pct for base metal, HW-TIG, A-TIG, and HLM weld compositions, respectively. Despite the fact that the formation of the $M_{23}C_6$ and sigma phases was predicted based on weld composition, experimental studies revealed no evidence of the presence of these phases. This is because these calculations are performed under equilibrium conditions; however, non-equilibrium cooling conditions predominate during welding. Nevertheless, after creep and thermal exposure, δ -ferrite transformed to the sigma phase, as revealed by microstructural examinations.

The microstructural degradation under creep exposure, such as sigma phase precipitation and cavitation at the interfaces due to mismatch in deformation, would lead to early initiation of the tertiary creep regime in the weld joints than the base metal. The higher creep

damage leading to early initiation of tertiary creep is clearly observed in the HW-TIG weld joint than in the other joints (Figure 11). Even though the sigma formation temperature is the same in all the cases (923 K), the higher fraction of sigma phase in the HW-TIG joint was observed. Among the weld joints, HW-TIG weld metal exhibited larger crack length ($154.9 \pm 6 \mu\text{m}$), cavity size ($25 \pm 7 \mu\text{m}$), and the number of cavities (~ 138 cavities/ mm^2) compared to A-TIG and HLM welds. The creep cavitation is predominantly lower in the case of HLM (76.9 cavities/ mm^2) and A-TIG (51.4 cavities/ mm^2) welds due to lower ferrite content. The crack length and cavity size in A-TIG and HLM weld joints were comparable, with a variation of ~ 20 pct. The initiation of creep cavities during the primary stage of creep exposure and its propagation to coalesce to form a macrocrack in the tertiary stage of creep would determine the creep rupture strength of the weld joints.^[7] In addition, the creep rupture strength of the weld joint is attributed to the combination of the following factors: (i) ferrite content, (ii) orientation of columnar

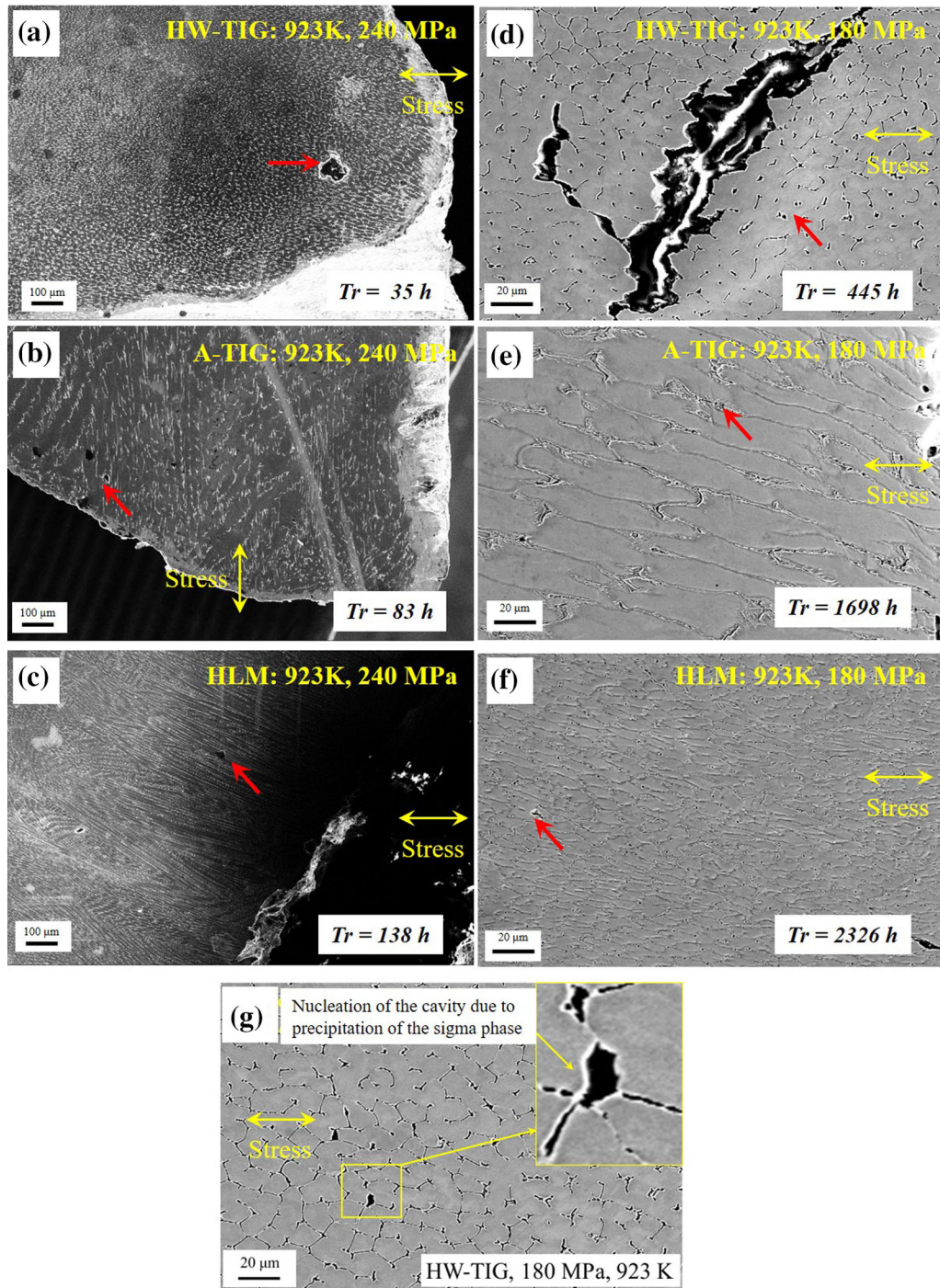


Fig. 20—SE micrograph showing the microstructural variation at the fracture end and cavity nucleation associated with sigma phase in (a, d) HW-TIG, (b, e) A-TIG, (c, f) HLM weld joints, and (g) showing the creep cavity in HW-TIG weld joint tested at 923 K.

dendrites/grains with loading axis, (iii) grain size/SDAS, (iv) morphology of δ -ferrite.

Further, the as-weld and creep rupture specimens were investigated using EBSD to evaluate the failure mechanism. Here, for the EBSD analysis, two stress

levels were considered, namely 240 and 180 MPa. The inverse pole figure (IPF) maps of the fusion zone region obtained from the as-weld condition, crept specimens (240 and 180 MPa), thermally exposed specimens with corresponding kernel average misorientation maps and

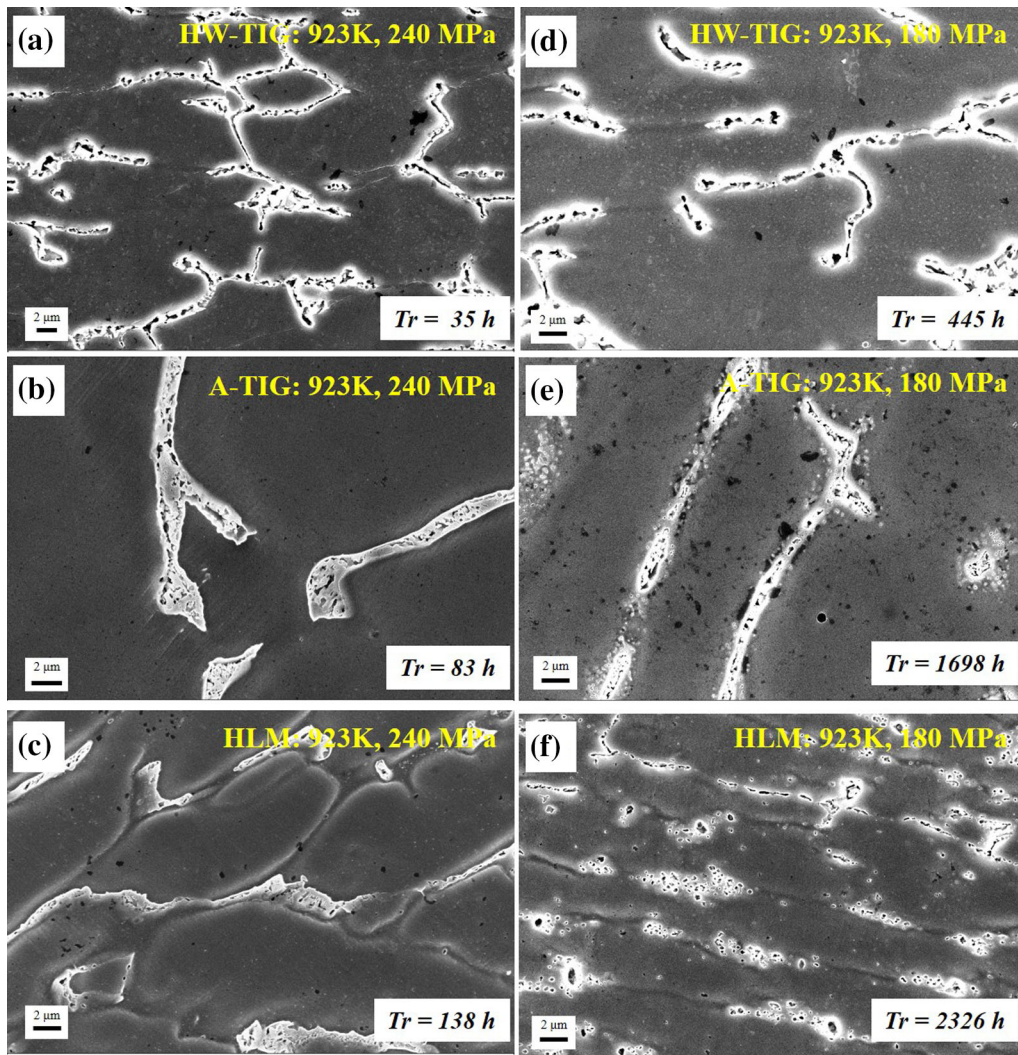


Fig. 21—SE micrographs showing the degradation of δ -ferrite in creep-exposed specimens of (a, d) HW-TIG, (b, e) A-TIG, and (c, f) HLM weld joints tested at 923 K.

different conditions of the structure are shown in Figures 26, 27, and 28(a) through (c). After creep tests, the EBSD scans were performed on the longitudinal section of the failed samples near the rupture location in all three weld joints. The IPF maps of as-weld condition and creep-tested specimens at 240 and 180 MPa clearly showed the variation in color contrast. This is ascribed to the orientation of substructures within a grain. The non-uniform color distribution in kernel average misorientation (KAM) maps (Figure 26(b)) depicts the accumulation of strains during welding (multiple thermal cycle process) and creep deformation. The microstructure of as-welded, creep, and thermally exposed weld joint specimens consists of recrystallized, substructure, and deformed regions (Figures 26, 27, and 28(c)). The proportion of these microstructural regions is found to change in the weld metal depending upon the thermal

cycles experienced during welding and exposure to thermal and creep conditions. In the as-welded condition, the fusion zone of HW-TIG and HLM joints exhibited a higher fraction of substructure than the A-TIG joint. However, a higher fraction of recrystallized (softer region) structure is observed in the A-TIG joint than in the HW-TIG and HLM joints. This is clearly evidenced in the variation of hardness in the fusion zone, where the lower hardness is observed in the fusion zone of A-TIG than in the HW-TIG and HLM weld metal regions. Higher hardness in the fusion zone of HW-TIG and HLM can be correlated with the higher strain observed in the HW-TIG and HLM KAM map than in the A-TIG. The higher deformed structure is observed in the HW-TIG creep rupture specimen tested at 240 MPa. This could be due to more interfaces such as grain boundary and austenite to ferrite interface.

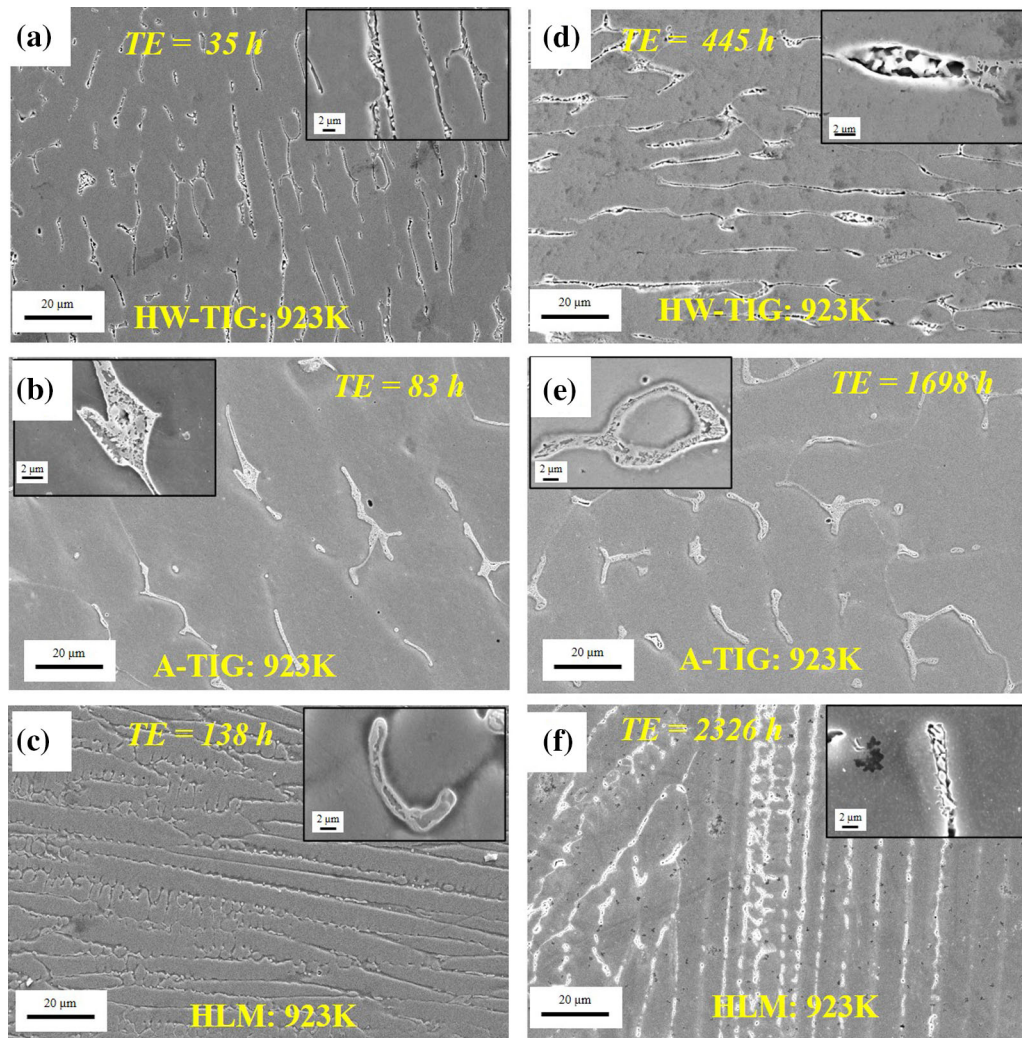


Fig. 22—SE micrograph showing the microstructural variation at thermally exposed (TE) specimens and microstructural degradation in (a, d) HW-TIG, (b, e) A-TIG, and (c, f) HLM weld joints tested at 923 K.

However, at lower stress (more prolonged creep exposure), the disintegration of δ -ferrite to sigma phase transformation leads to a reduction in interface regions and an increase in the frequency of recrystallized and substructure structures in the HW-TIG joint. Hence, a lower frequency of the deformed structure and a higher frequency of recrystallized structure are observed in the HW-TIG joint than in the A-TIG and HLM joints. The higher frequency of substructures could be seen in all the weld joints. In the case of HLM and A-TIG weld joints, the columnar dendrites were aligned along the loading direction, and the number of interfaces was relatively lower than HW-TIG welds, which resulted in the higher frequency of substructures at both stress levels. The higher deformed structure in the crept (180 MPa) A-TIG joint depicts the dominance of higher work hardening than the creep cavitation damage during

creep. At higher stress levels, the creep failure can be attributed to a high rate of deformation with a minor contribution from the phase transformation of δ -ferrite. However, the creep rupture can be primarily attributed to the phase transformation at lower stresses. It should be noted that δ -ferrite is rich in Cr and Mo, and the diffusion of these elements is faster due to its bcc structure, and external stress provides additional diffusion paths to facilitate the transformation. These ferrite-stabilizing elements are sufficient for the formation of the intermetallic sigma phase under prolonged thermal or creep exposure. The transformed brittle intermetallic sigma phases distributed in the austenite matrix experience strength mismatch during creep deformation. Therefore, strain accumulation can be seen near the austenite/ δ -ferrite (transformed to sigma) interfaces, as revealed by KAM maps. This strength

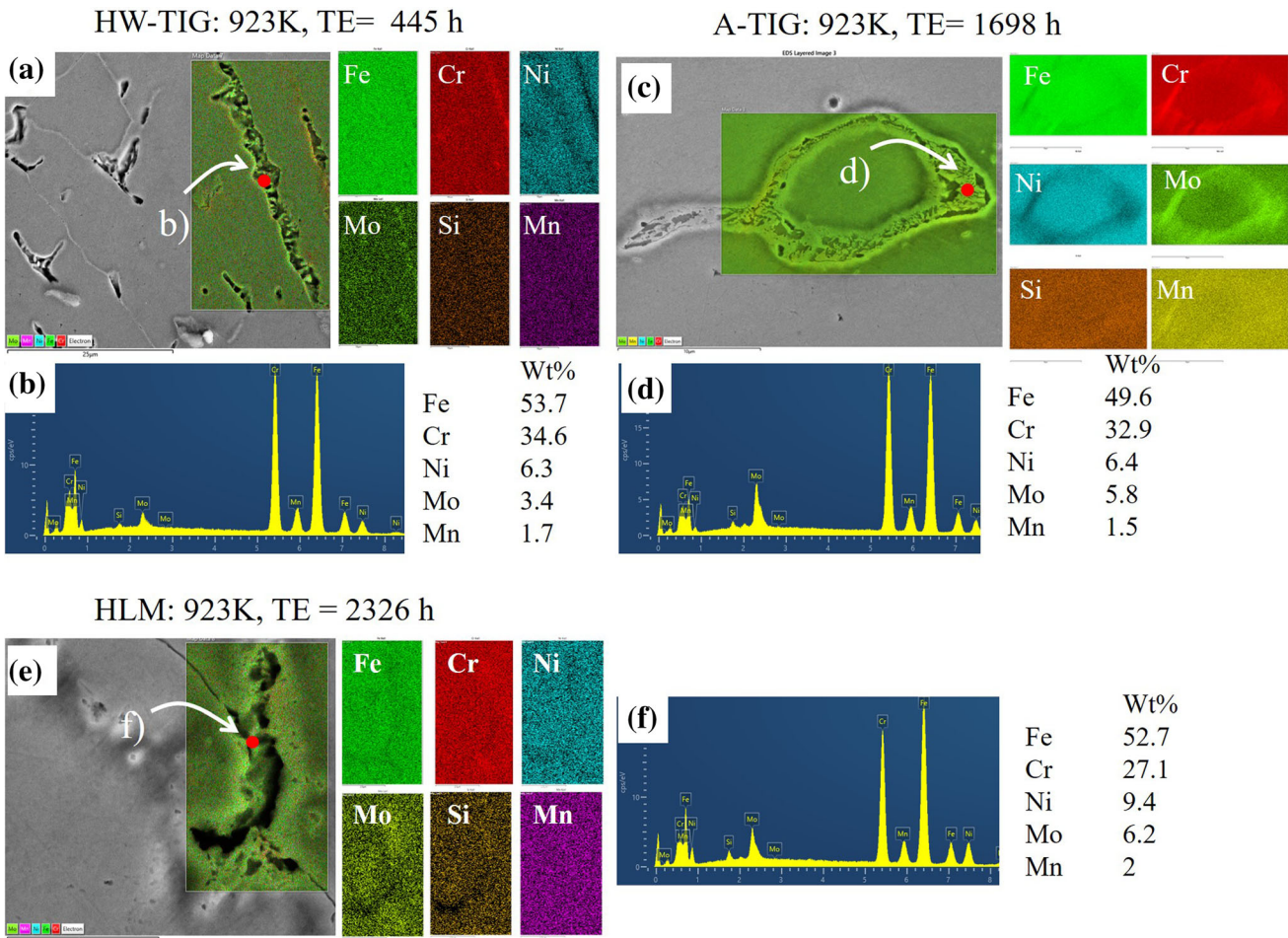


Fig. 23—EDS elemental mapping and spectra obtained for thermally exposed (TE) (923 K) (a, b) HW-TIG, (c, d) A-TIG, and (e, f) HLM weld joints.

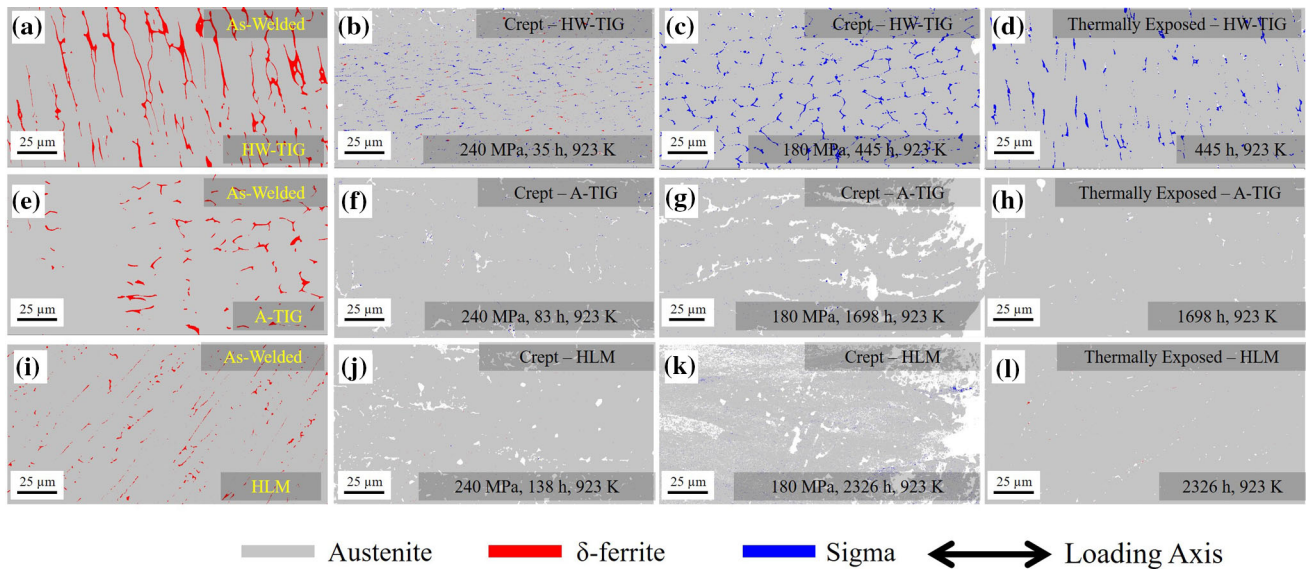


Fig. 24—EBSD phase map showing the phase transformation of δ -ferrite to sigma phase under creep and thermal exposure in the fusion zone of weld joint fabricated using (a through d) HW-TIG, (e through h) A-TIG, and (i through l) HLM welding processes tested at 923 K.

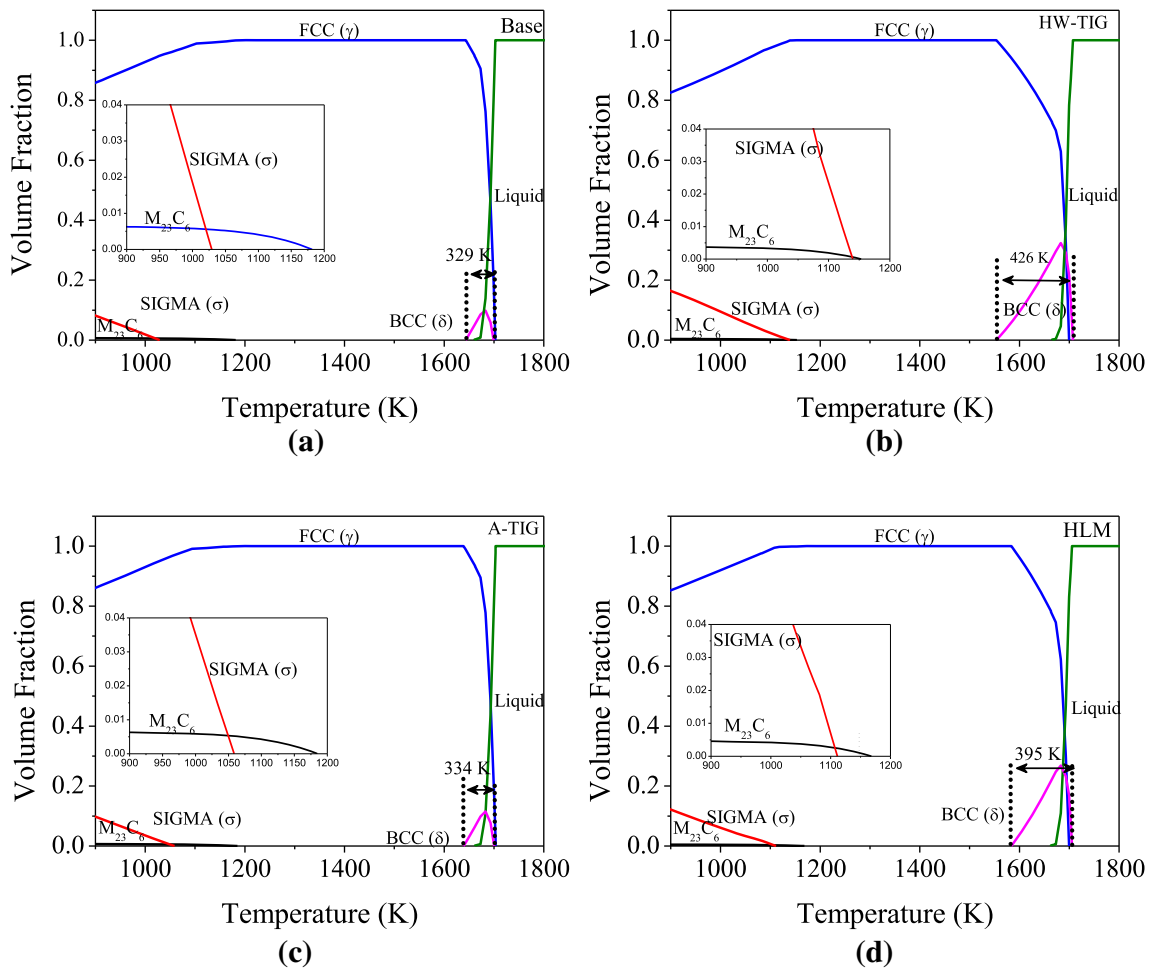


Fig. 25—The calculated equilibrium phase fraction of (a) base material, (b) HW-TIG, (c) A-TIG, and (d) HLM weld joint composition predicted by Thermo-Calc software.

mismatch eventually results in the nucleation and propagation of cavities at the interface to cause failure. It is evident that isolated δ -ferrite was observed in A-TIG and HLM welds, while interconnected δ -ferrite was observed in HW-TIG welds. The phase transformation is faster in HW-TIG welds because the Cr and Mo get an easy diffusion path in interconnected δ -ferrite compared to A-TIG and HLM welds. In addition, A-TIG and HLM welds presented lower ferrite content than that of HW-TIG welds. This discussion clearly reveals that the premature failure of weld joints is primarily due to the δ -ferrite content.

A weld strength reduction factor (WSRF) is added to the base material data when designing the components of Fast Breeder Reactor to account for the decrease in creep strength of the weld joint. The WSRFs are defined by RCC-MR code^[29] as the ratio of uniaxial weld joint creep rupture strength to uniaxial base metal creep rupture strength. Figure 29 illustrates the changes in

WSRF of weld joints with rupture life at 923 K and compares them to the value recommended in the RCC-MR code for 316LN austenitic stainless steel.^[21] All the weld joints exhibited superior WSRF than that of RCC-MR recommended data. Among the weld joints, HLM and A-TIG displayed stable WSRF as a function of time, while the WSRF of HW-TIG weld joint decreased with rupture life. Overall, the excellent creep rupture strength of the HLM weld joint over the other joints can be attributed to lower δ -ferrite content, lower proportion of fusion zone area, and columnar dendrites oriented along the loading direction. A-TIG weld joint exhibited relatively lower creep strength than HLM weld joint due to higher HAZ width, higher fusion zone area, and higher ferrite content. In contrast, HW-TIG weld joints displayed poorer creep rupture strength than A-TIG and HLM weld joints. This is primarily due to the heterogeneous microstructure and higher δ -ferrite content.

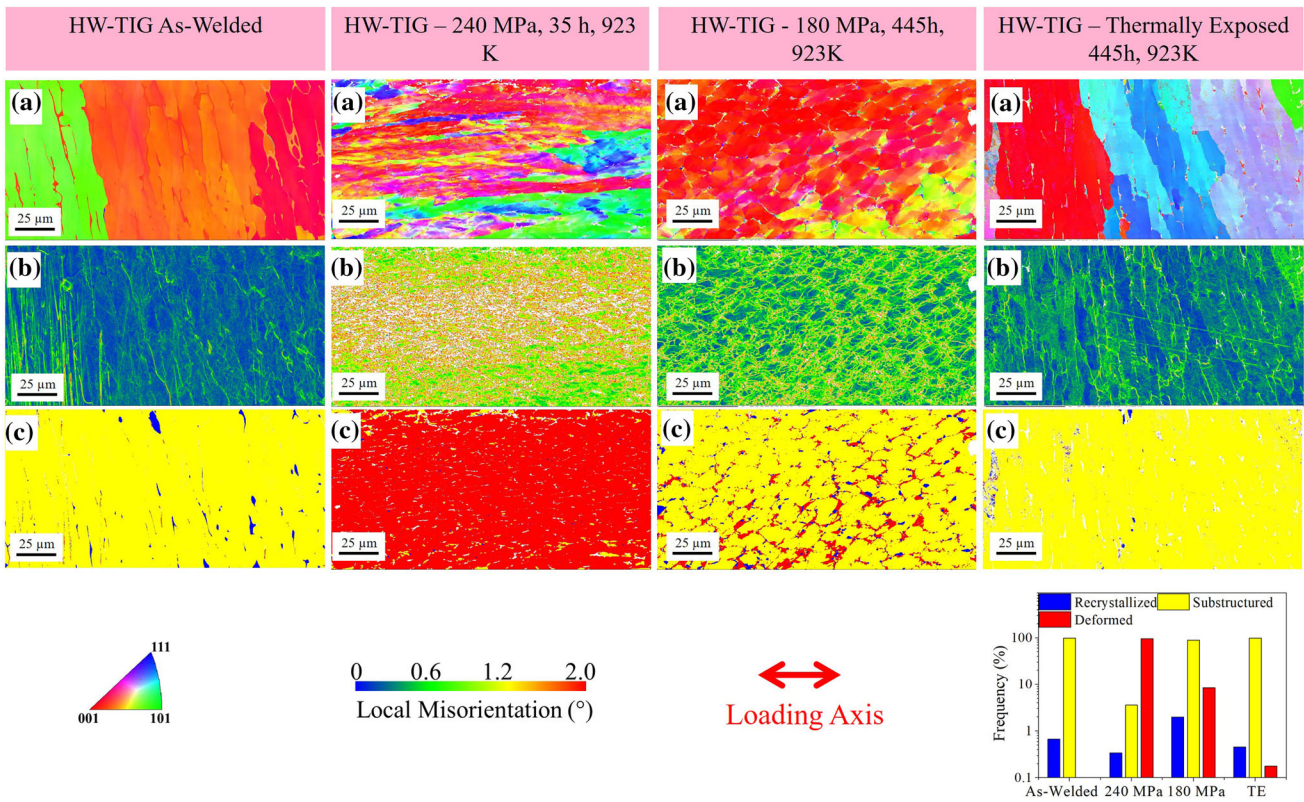


Fig. 26—(a) EBSD-IPF map, (b) KAM map describing the strain distribution, and (c) recrystallized, substructure, deformed grains of HW-TIG as-weld specimens, creep rupture specimens (240 and 180 MPa), and thermally exposed specimens.

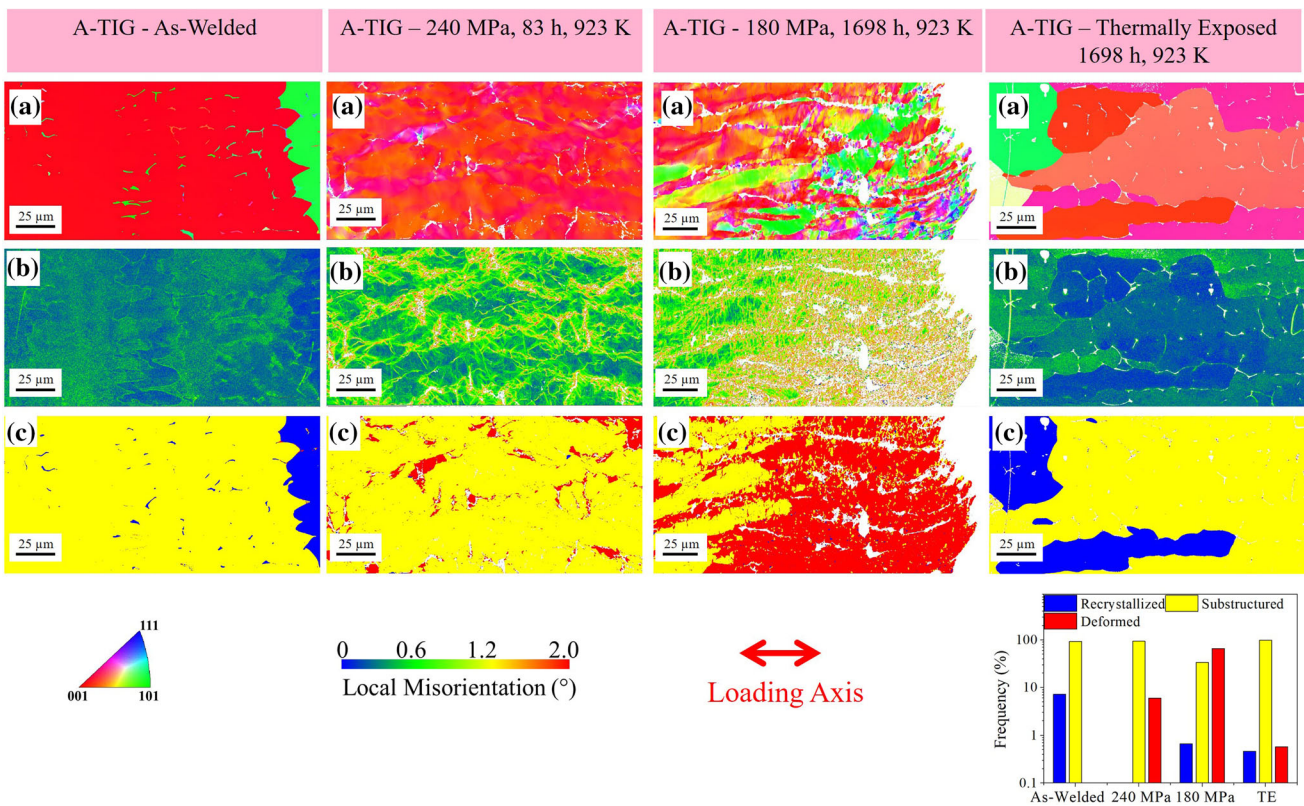


Fig. 27—(a) EBSD-IPF map, (b) KAM map describing the strain distribution and (c) recrystallized, substructure, deformed grains of A-TIG as-weld specimens, creep rupture specimens (240 and 180 MPa), and thermally exposed specimens.

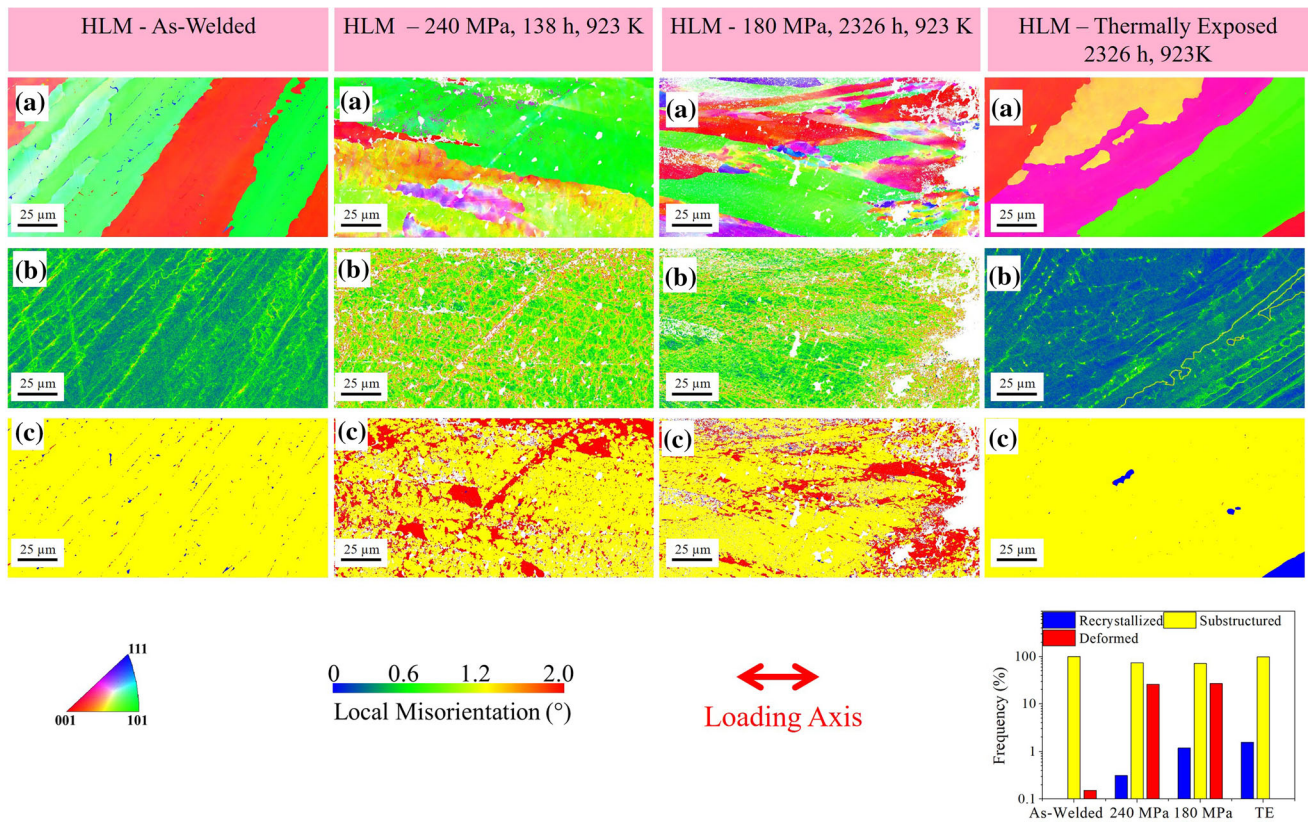


Fig. 28—(a) EBSD-IPF map, (b) KAM map describing the strain distribution, and (c) recrystallized, substructure, deformed grains of HLM as-weld specimens, creep rupture specimens (240 and 180 MPa), and thermally exposed specimens.

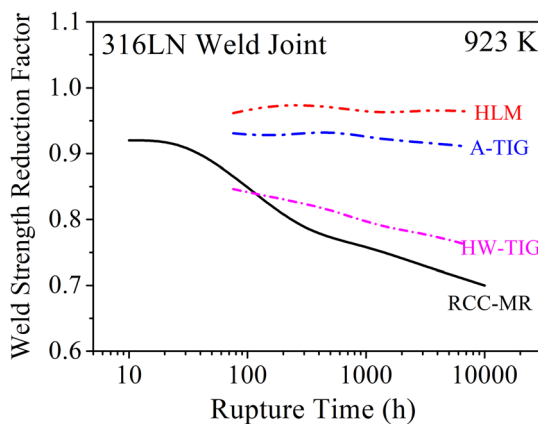


Fig. 29—Weld strength reduction factors (WSRFs) estimated for HW-TIG, A-TIG, and HLM joints were compared with recommended RCC-MR data.

IV. CONCLUSIONS

The creep deformation and rupture behavior of the 11-mm-thick type 316LN weld joints fabricated by HW-TIG, A-TIG, and HLM welding processes were investigated at 923 K. The salient findings from this study are summarized as follows.

1. The welding process significantly influenced the δ -ferrite content in the weld joints [A-TIG (1.7 FN), HLM (1.3 FN), and HW-TIG (3.5)] and its

morphology. The HW-TIG and HLM weld joints showed higher hardness than the A-TIG weld joint due to tensile residual stresses and strain hardening caused during subsequent weld passes.

2. Heterogenous microstructure resulted in localized creep deformation in the weld joints. In addition, the degradation of δ -ferrite to sigma phase and further cavitation due to strength mismatch significantly influenced the rupture behavior of the weld joints. The HW-TIG weld joint showed significantly higher creep cavities (138 cavities/mm²) than A-TIG (51 cavities/mm²) and HLM (76 cavities/mm²) weld joints.
3. The weld joints exhibited lower creep rupture life than the base material. Among the weld joints, HLM and A-TIG weld joints showed significantly higher creep rupture life. The creep rupture life of the weld joints exhibited a good correlation with the ferrite content and revealed the creep rupture life in the following order: HW-TIG < A-TIG < HLM.
4. The kernel average misorientation maps reveal the strain accumulation at the ferrite-austenite interfaces that results in the nucleation of creep cavities.
5. The relatively higher deformed structure in the A-TIG and HLM than the HW-TIG weld joint depicts the dominance of higher work hardening than the creep cavitation damage at prolonged creep exposure. At higher stress levels, the creep failure can be attributed to high rate deformation

with a minor contribution from the phase transformation of δ -ferrite.

- All the weld joints showed a higher weld strength reduction factor (WSRF) than the recommended RCC-MR code. In comparison, the HLM weld joint exhibited better WSRF than the HW-TIG and A-TIG weld joints.
- HLM weld joints manifested predominantly higher creep rupture strength than A-TIG (~ 25 to 45 pct) and HW-TIG (~ 80 pct) weld joints. Therefore, HLM welding is recommended over A-TIG and HW-TIG welding processes for joining thick (greater than 10 mm) 316LN stainless steel components.

ACKNOWLEDGMENTS

The authors acknowledge Dr. Arup Dasgupta, Head, Physical Metallurgy Division, Indira Gandhi Centre for Atomic Research (IGCAR), India, for providing the EBSD Facility. Dr. S. Mahadevan and Shri. S. Arun Kumar are earnestly acknowledged for residual stress measurements using the X-ray diffraction technique and fruitful discussions during this work.

CONFLICT OF INTEREST

On behalf of all authors, the corresponding author states that there is no conflict of interest.

REFERENCES

- A.K. Bhaduri, K. Laha, V. Ganesan, T. Sakthivel, M. Nandagopal, G.V.P. Reddy, J.G. Kumar, V.D. Vijayanand, S.P. Selvi, G. Srinivasan, C.R. Das, A. Nagesha, S. Ravi, P. Parameswaran, R. Sandhya, and S.K. Albert: *Int. J. Press. Vessel Pip.*, 2016, vol. 139–140, pp. 123–36.
- B. Arivazhagan and M. Vasudevan: *J. Manuf. Process.*, 2015, vol. 18, pp. 55–59.
- M. Vasudevan: PhD Thesis, Indian Institute of Technology, Chennai, India.
- T. Sakthivel, M. Vasudevan, K. Laha, P. Parameswaran, K.S. Chandravathi, M.D. Mathew, and A.K. Bhaduri: *Procedia Eng.*, 2013, vol. 55, pp. 408–13.
- R.G. Berggren, N.C. Cole, G.M. Goodwin, J.O. Stiegler, G.M. Slaughter, R.J. Gray, and R.T. King: *Weld. J.*, 1978, vol. 57, pp. 167s–174s.
- R.G. Thomas: *Weld. J.*, 1978, vol. 57, pp. 1–6.
- G. Sasikala, S.L. Mannan, M.D. Mathew, and K.B. Rao: *Metall. Mater. Trans. A*, 2000, vol. 31A, pp. 1175–85.
- G. Sasikala, S.K. Ray, and S.L. Mannan: *Acta Mater.*, 2004, vol. 52, pp. 5677–86.
- K. Hori, K. Kusano, and T. Myoga: *Weld. Int.*, 2004, vol. 18, pp. 456–68.
- M. Vasudevan: *J. Mater. Eng. Perform.*, 2017, vol. 26, pp. 1325–36.
- T. Sakthivel, M. Vasudevan, K. Laha, P. Parameswaran, K.S. Chandravathi, M.D. Mathew, and A.K. Bhaduri: *Mater. Sci. Eng. A*, 2011, vol. 528, pp. 6971–80.
- C. Fang, J. Xin, W. Dai, J. Wei, J. Wu, and Y. Song: *J. Laser Appl.*, 2020, vol. 32, p. 012009.
- X.N. Wang, S.H. Zhang, J. Zhou, M. Zhang, C.J. Chen, and R.D.K. Misra: *Opt. Lasers Eng.*, 2017, vol. 91, pp. 86–96.
- J. Yan, M. Gao, and X. Zeng: *Opt. Lasers Eng.*, 2010, vol. 48, pp. 512–17.
- P.L. Moore, D.S. Howse, and E.R. Wallach: *Sci. Technol. Weld. Join.*, 2004, vol. 9, pp. 314–22.
- A.R. Pavan, N. Chandrasekar, B. Arivazhagan, S. Kumar, and M. Vasudevan: *CIRP J. Manuf. Sci. Technol.*, 2021, vol. 35, pp. 675–90.
- A.R. Pavan, B. Arivazhagan, M. Vasudevan, and S. Govind Kumar: *CIRP J. Manuf. Sci. Technol.*, 2022, vol. 39, pp. 294–307.
- A.R. Pavan, B. Arivazhagan, G.K. Sharma, S.A. Kumar, S. Mahadevan, and M. Vasudevan: *J. Mater. Eng. Perform.*, 2022, <https://doi.org/10.1007/s11665-022-06654-2>.
- S. Kou: *Welding Metallurgy*, Wiley, Hoboken, 2003.
- M. Ragavendran and M. Vasudevan: *Mater. Manuf. Process.*, 2020, vol. 35, pp. 922–34.
- M.D. Mathew, S. Latha, and K.B.S. Rao: *Mater. Sci. Eng. A*, 2007, vol. 456, pp. 28–34.
- V. Shankar, T.P.S. Gill, S.L. Mannan, and S. Sundarlsan: *Sadhana Acad. Proc. Eng. Sci.*, 2003, vol. 28, pp. 359–82.
- A. Elmesalamy, J.A. Francis, and L. Li: *Int. J. Press. Vessel Pip.*, 2014, vol. 113, pp. 49–59.
- D.R. Bajic, M.M. Savitsky, G.M. Melnichuk, and A.F. Lupan: *Pat. Weld. J. C/C Avtom. SVARKA*, 2002, vol. 9, pp. 30–34.
- K.R. Gadelrab, G. Li, M. Chiesa, and T. Souier: *J. Mater. Res.*, 2012, vol. 27, pp. 1573–79.
- M. Ragavendran, M. Vasudevan, and N. Hussain: *J. Mater. Eng. Perform.*, 2022, <https://doi.org/10.1007/s11665-021-06534-1>.
- S.L. Mannan and M.D. Mathew: *Bull. Mater. Sci.*, 1996, vol. 19, pp. 985–1007.
- M.D. Mathew, K. Laha, and V. Ganesan: *Mater. Sci. Eng. A*, 2012, vol. 535, pp. 76–83.
- RCC-MR, *Design and Construction Rules for Mechanical Components for FBR Nuclear Islands, Section I-Subsection Z, Appendix 3*, 1985.
- B.A. Senior: *J. Mater. Sci.*, 1990, vol. 25, pp. 45–53.
- J.J. Smith and R.A. Farrar: *Int. Mater. Rev.*, 1993, vol. 38, pp. 25–51.
- B. Weiss and R. Stickler: *Metall. Mater. Trans. B*, 1972, vol. 3B, pp. 851–66.
- J.K. Lai and A. Wickens: *Acta Metall.*, 1979, vol. 27, pp. 217–30.
- C.-C. Hsieh and W. Wu: *ISRN Metall.*, 2012, vol. 2012, pp. 1–16.
- A.F. Padilha, D.M. Escriba, E. Materna-Morris, M. Rieth, and M. Klimenkov: *J. Nucl. Mater.*, 2007, vol. 362, pp. 132–38.
- T. Sakthivel, M. Vasudevan, K. Laha, P. Parameswaran, K.S. Chandravathi, M.D. Mathew, and A.K. Bhaduri: *J. Nucl. Mater.*, 2011, vol. 413, pp. 36–40.
- M. Ragavendran, J.G. Kumar, and M. Vasudevan: *Mater. Sci. Eng. A*, 2022, vol. 832, p. 142445.

Publisher's Note Springer Nature remains neutral with regard to jurisdictional claims in published maps and institutional affiliations.

Springer Nature or its licensor (e.g. a society or other partner) holds exclusive rights to this article under a publishing agreement with the author(s) or other rightsholder(s); author self-archiving of the accepted manuscript version of this article is solely governed by the terms of such publishing agreement and applicable law.